Electron transport during shock ignition

Contact *t.bell1@physics.ox.ac.uk*

AR Bell

Clarendon Laboratory, University of Oxford, Parks Road, Oxford UK OX1 3PU

Shock ignition (Betti et al, 2007, 2008; Ribeyre et al 2009) is one of the most promising routes to commercially viable inertial fusion energy (IFE). Compression is achieved on a low adiabat with minimum energy input. Once compressed, a strong shock is launched into the target by a high power laser. The shock converges on the centre of the target, heating the target and initiating burn.

We show here, with an idealized self-similar calculation, that laser interaction with dense targets during shock ignition can be separated into two regimes. In the ablative regime, corresponding to conditions found in conventional directly driven IFE, the interaction relaxes to a quasi-steady balance between electron thermal conduction carrying energy to high density and hydrodynamic energy flux (ablative enthalpy flow) which carries energy away from high density. In contrast, at high laser intensity, the heat flow Q into the target is too great to be balanced by hydrodynamic flow. In this regime, the structure is that of a supersonic heat front with very little hydrodynamic response.

In a calculation assuming that the Spitzer conductivity is acceptably valid, we show that conditions during shock ignition straddle the boundary between these two regimes. When reduced to its bare essentials, the laser-plasma interaction can be represented by 1D perfect gas fluid equations for mass, momentum and energy with additional energy fluxes carried by the laser and by Spitzer conduction (I and $Q=-\kappa\mathrm{grad}(T)$ respectively).

To derive a self-similar solution to the fluid equations the dependence of the conductivity on the fluid variables is required. The Spitzer conductivity is determined by the mean free path λ of electrons as can be shown by writing the Spitzer heat flow as $Q=q(\lambda/L)Q_f$, where L is the temperature scalelength $L=T/\mathrm{grad}(T)$. $Q_f= n_e k_B T(k_B T/m_e)^{1/2}$ is the free-streaming heat flow, and q is a numerical factor of order unity. For Coulomb collisions, λ is proportional to T^2 and this results in a self-similar solution which depends on the similarity variable $s=x/t^{4/3}$. ρ, u, P, Q & I can then be written as functions of s times a power of the ratio of time t to some characteristic time t_0:

$$\rho=\rho(s) \quad ; \quad \mathrm{u}=\mu(s)\left(\frac{t}{t_0}\right)^{1/3} \quad ; \quad P=\rho(s)\varphi(s)\left(\frac{t}{t_0}\right)^{2/3}$$

$$Q=-\left(\frac{\kappa_0}{t_0^{4/3}}\right)\varphi^{5/2}\frac{\partial\varphi}{\partial s}\left(\frac{t}{t_0}\right) \quad ; \quad I=\varepsilon(s)\left(\frac{t}{t_0}\right)$$

where κ_0 is a constant determining the magnitude of the Spitzer heat flow. ε is the self-similar laser energy flux. For laser energy absorption at a particular position s_{abs}, with a delta function energy input to the plasma where the density is ρ_{abs}, ε is a constant for $s<s_{abs}$, and $\varepsilon=0$ for $s>s_{abs}$. The self-similar hydro equations in the overdense plasma ($I=0$) are then:

$$\frac{\partial}{\partial s}(\rho\mu)=\frac{4}{3}t_0^{1/3}s\frac{\partial\rho}{\partial s}$$

$$\frac{\partial}{\partial s}(\rho\mu^2+\rho\varphi)=\frac{4}{3}t_0^{1/3}s\frac{\partial(\rho\mu)}{\partial s}$$

M Tzoufras

Clarendon Laboratory, University of Oxford, Parks Road, Oxford UK OX1 3PU

$$\frac{\partial}{\partial s}\left(\frac{5}{2}\rho\varphi\mu+\frac{1}{2}\rho\mu^3-\left(\frac{\kappa_0}{t_0^{4/3}}\right)\varphi^{5/2}\frac{\partial\varphi}{\partial s}\right)=\frac{4}{3}t_0^{1/3}s\frac{\partial}{\partial s}\left(\frac{3}{2}\rho\varphi+\frac{1}{2}\rho\mu^2\right)$$

As expected, all quantities are now a function of one variable, s, instead of two, x & t. We find that not only are all quantities functions of s alone, but there is only one numerical constant, $\kappa_0/t_0^{4/3}$. This constant determines the ratio of energy flux by thermal conduction to energy flux by hydrodyamic motion and whether the solution lies in the ablative or heat flow regime. In the self-similar solution, the laser intensity rises linearly in time, and the rate of rise determines the numerical constant $\kappa_0/t_0^{4/3}$.
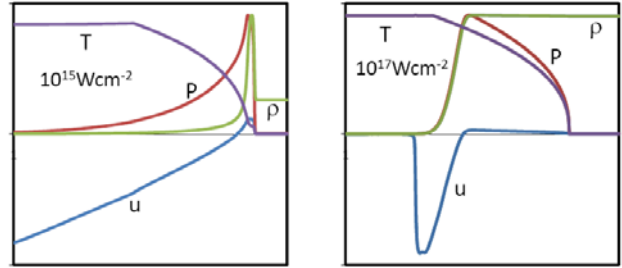

Figure 1. Profiles at 10^{15}Wcm^{-2} after 100ps and 10^{17}Wcm^{-2} after 1psec (arbitrary units)

Figure 1 shows how the laser-plasma interaction changes from the ablation regime at an absorbed laser intensity of 10^{15}Wcm^{-2} to a supersonic electron heat front at 10^{17}Wcm^{-2}. At both intensities the laser wavelength is $1/3\mu$m and absorption takes place at the critical density. The dense part of the target, at the right hand boundary, is initialised at 1 gm cm^{-3}. The laser intensity reaches the specified intensity at the end of a laser pulse of duration τ. The total laser energy is made the same at each laser intensity by choosing a pulse duration inversely proportional to the laser intensity such that in the left hand graph in the figure the intensity reaches 10^{15}Wcm^{-2} after 100psec, whereas in the right hand graph the intensity reaches 10^{17}Wcm^{-2} after only 1 psec. At 10^{15}Wcm^{-2}, the base of the temperature front coincides with the surface of the high density plasma. The high pressure launches a shock into the dense plasma and causes plasma to ablate from the surface. In contrast at 10^{17}Wcm^{-2}, the temperature front penetrates supersonically into the dense plasma with very little time for the plasma to start expanding from the surface.

Figure 2 plots the variation of the maximum pressure with laser intensity. At low intensity, the maximum pressure is proportional to laser intensity to the power 2/3 as expected for the ablation regime. At high intensity, the pressure is proportional to intensity to the power 2/9 as can easily be derived for a supersonic electron heat front. Figure 2 indicates that shock ignition lies at about the transition point between the two regimes, although the complicated density structures at the end of the compression phase must be taken account of for a realistic calculation, and non-local transport may affect the results.
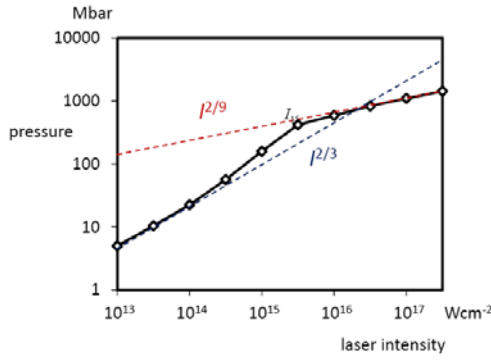
Figure 2. Pressure against intensity with the Spitzer conductivity

We assess the effect of non-local transport by time-dependent solution of the Vlasov-Fokker-Planck (VFP) equation self-consistently coupled to the perfect gas fluid equations. This amounts to replacing the Spitzer conduction equation with the VFP equation in our set of equations. The VFP equation for the electron distribution function $f(z,\mathbf{v},t)$ in one planar dimension, z, is

$$\frac{\partial f}{\partial t} + \mathbf{v}_z \frac{\partial f}{\partial z} - eE \frac{\partial f}{\partial \mathbf{v}_z} = C(f) + S(f)$$

where $C(f)$ is the collision term and $S(f)$ models laser absorption. The electric field is determined implicitly to produce zero electron current in the ion rest frame and maintain neutrality. The code uses the KALOS formalism (Bell et al 2006), which expands the distribution function in spherical harmonics. We find it sufficient for this problem to restrict the harmonic expansion to zeroth and first order, otherwise known as the diffusive approximation, which is equivalent to writing f as

$$f(z,\mathbf{v},t) = f_0(z,|\mathbf{v}|,t) + f_1(z,|\mathbf{v}|,t)\frac{\mathbf{v}_z}{|\mathbf{v}|}$$

Momentum is transferred from electrons to ions through the electric field and by collisions. The ion thermal capacity is smaller than electron thermal capacity by the ionization Z, here taken to be 4. Consequently we treat the ions as cold and ignore collisional energy transfer between electrons and ions. The electron distribution f is defined in the ion rest frame to simplify the collision term $C(f)$. The local ion velocity u varies in space. To allow for this, extra terms are added to the VFP equation as set out in equation 1 of Bell 1985. These terms are relatively small because the ion velocity is much smaller than the electron thermal velocity, but they are important because they include adiabatic cooling during rarefaction.

The dominant collision term is the angular scattering of electrons by ions which causes f_1 to decay exponentially. The electron-electron collision term takes the form of an advection-diffusion equation in momentum. The well-established approximation is made that the collision integrals, which are the equivalent of the Rosenbluth potentials, are calculated purely from the isotropic part of the distribution f_0 and a correction made to conserve momentum. The collision term is non-linear in the distribution function so we solve iteratively to conserve both electron number and electron energy to any prescribed accuracy down to rounding error.

At laser intensities of interest, collisionless absorption may be important, so energy is absorbed in a region surrounding the critical density by removing a fraction of the electron distribution each timestep and replacing it with an isotropic Maxwellian at a temperature $T_e + T_{hot}$ where T_e is the electron temperature (defined in terms of the mean electron energy) at the start of the timestep and T_{hot} is a hot electron temperature

specified in line with experimental data (Gitomer et al, 1986, Beg et al, 1997). The fraction replaced is chosen to give the required energy absorption.

We solve the VFP-hydro equations with a laser intensity rising linearly with time. This is equivalent to the self-similar calculation used above with the Spitzer-hydro equations except that it is not possible to begin the calculation with zero temperature or a step discontinuity in density at the critical surface. Nevertheless, the solution approaches the self-similar solution at the end of the calculation giving a meaningful comparison with the Spitzer-hydro results for the importance of non-local effects. For self-similarity the hot electron temperature T_{hot} varies in proportion to $t^{2/3}$, which makes $T_{hot} = \alpha I^{2/3}$ where α is chosen so that T_{hot} takes the required value at the end of the calculation.
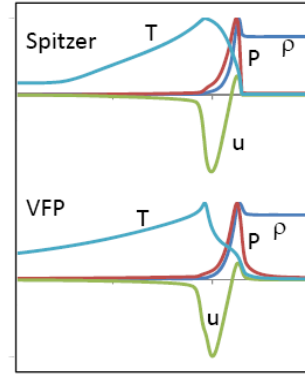
Figure 3. Spitzer and VFP ablation profiles at 10^{16}Wcm^{-2}

The profiles of temperature, velocity, density and pressure are shown in figure 3 for VFP and Spitzer calculations at an intensity of 10^{16}Wcm^{-2}. The VFP temperature profile is concave rather than convex. The pressure profiles differ little except that a VFP pressure precursor extends into the high density plasma due to the long mean free path of the more energetic part of the electron distribution.
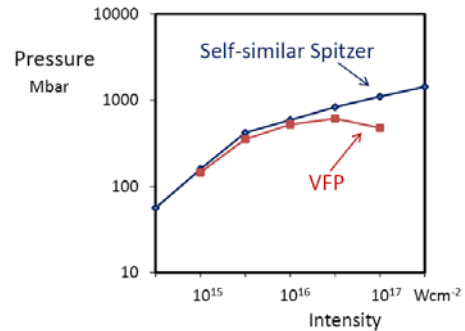
Figure 4. Pressure against intensity for VFP and Spitzer

As seen in figure 4, the VFP pressure only departs from the Spitzer pressure at high intensities well into the heat front regime. This is consistent with the conclusion from figure 3 that even if the VFP and Spitzer temperature profiles are different, the ablation process compensates for moderate intensities to give a similar pressure profile.

References

Beg FN et al, Phys Plasmas **4**, 447 (1997)
Bell AR, Phys Fluids **28**, 2007 (1985)
Bell AR et al, Plasma Phys Control Fusion **48**, R37 (2006)
Betti R et al, Phys Rev Lett **98**, 155001 (2007)
Betti R et al, JPhys conf series **112**, 022024 (2008)
Gitomer SJ et al, Phys Fluids **29**, 2679 (1986)
Ribeyre X et al, Plasma Phys Control Fusion **51**, 015013 (2009)

New perspectives on the electrodynamics of intense laser-plasmas

DA Burton

*Department of Physics, Lancaster University, UK
& The Cockcroft Institute, Daresbury Science and Innovation
Campus, Daresbury, Warrington, UK*

RW Tucker

*Department of Physics, Lancaster University, UK
& The Cockcroft Institute, Daresbury Science and Innovation
Campus, Daresbury, Warrington, UK*

Main contact email address:	d.burton@lancaster.ac.uk

High-power lasers provide novel avenues for controllable investigation of matter in extreme conditions that only occur naturally away from the Earth. Moreover, it is expected that the next generation of ultra-intense lasers will, for the first time, allow controllable access to regimes where a host of different quantum electrodynamic phenomena will be evident [1]. The behaviour of intense laser-plasmas in such regimes is complex, and effective models will be indispensable for elucidating the influence of the quantum vacuum. In particular it is expected that semi-classical field theories, for example theories that include the Euler-Heisenberg Lagrangian [2], will play an important role and a key feature of such theories is that they are fundamentally non-linear. Virtual electron-positron pairs associated with the quantum vacuum provide an effective non-linear medium in which the electromagnetic field propagates.

Born-Infeld electrodynamics [3] has enjoyed a renaissance in recent years [4-7]. Unlike their Maxwell counterparts, the Born-Infeld field equations are fundamentally non-linear at the classical level; they are non-linear even in the classical vacuum. One can encode the vacuum Born-Infeld field equations in terms of non-linear constitutive relations expressing the electric displacement **D** and magnetic field **H** in terms of the electric field **E** and magnetic induction **B**, leading to profound differences in the predictions of the Maxwell and Born-Infeld theories. In particular, Born and Infeld introduced their theory in order to ameliorate the singular self-energy of a classical point charge. However, it was also discovered that among the family of non-linear generalizations of Maxwell electrodynamics, Born-Infeld theory shares some highly attractive features with Maxwell theory; in particular, like the vacuum Maxwell equations, the vacuum Born-Infeld equations exhibit zero birefringence and its solutions have exceptional causal behaviour [8,9]. Moreover, Born-Infeld theory shares a number of properties with the low energy dynamics of strings and branes [10], and one can speculate that it may be more fundamental than Maxwell electrodynamics. If correct, this would revolutionize electrodynamics and have significant implications for the notorious problem of determining the classical force on a single accelerating point charge due to its own electromagnetic field, which has remained unresolved for over a century. Dirac [11] employed classical Maxwell electrodynamics, energy-momentum conservation and mass regularization to develop the Lorentz-Dirac equation of motion for an accelerating point electron which, unless special conditions are adopted for the final state of the electron, predicts that a classical free electron in vacuo can self-accelerate and the electron may experience a sudden acceleration before it enters a region of space containing a non-vanishing external electrostatic field.

As noted earlier, a host of different QED phenomena will be accessible to the next generation of intense lasers and non-linear electrodynamics in the context semi-classical QED will be central to their study. However, we speculate that Born-Infeld electrodynamics may play a role before it is necessary to invoke QED and this might become apparent in laser-plasma experiments over the next decade. Born-Infeld theory is characterized by a new fundamental constant of nature which limits the magnitude of the electric field of a static point charge.

To explore this further, we recently initiated a programme of work to elucidate the ramifications of Born-Infeld electrodynamics for high-field laser interactions with matter. In particular, we showed in [6] that a plane electromagnetic wave in a constant magnetic field propagates with a phase speed less than the speed of light in the vacuum and that this might be detectable in a terrestrial experiment. We also explored the behaviour of large amplitude electrostatic waves in a cold Born-Infeld plasma [7]. It is well-known that the amplitude of a plane longitudinal quasi-static oscillation of a relativistic cold Maxwell plasma is bounded from above (the so-called "wave-breaking" limit) [12,13], and the maximum electric field diverges as the phase velocity of the wave tends to the speed of light. We determined the corresponding maximum electric field in a cold Born-Infeld plasma and showed that it is bounded from above by the reciprocal of the Born-Infeld fundamental constant [7]. Furthermore, we extracted the Born-Infeld correction to the period of the wave in the ultra-relativistic regime of a cold Maxwell plasma.

In the high energy regime in which relativistic effects dominate – such as laboratory based laser-plasma acceleration – plasmas are commonly described by the collisionless Vlasov equation. An analysis of wave-breaking in warm Maxwell plasmas that directly employs distributional solutions to the Vlasov equation was given recently [14]. Alternatively, one may describe warm plasmas using the velocity moments of a one-particle distribution function. It is common to assume that the infinite hierarchy of field equations, obtained from velocity moments of the Vlasov equation, may be truncated to yield a closed set of field equations and a novel geometric averaging procedure for constructing velocity moments was recently developed [15-17] and used to establish rigorous conditions for the validity of the truncation in the ultra-relativistic regime. Recent work has also focussed on geometrical constructions of distributional solutions to the Maxwell-Vlasov system [18].

The collisionless approximation is often justified as the timescales governing relativistic processes in an underdense plasma are typically much shorter than the average time between collisions. However, recent advances in high energy density science have increased the demand for efficient descriptions of plasma dynamics fully incorporating both relativistic and collisional effects. Although the relativistic Fokker-Planck equation describes collisional plasmas in the relativistic regime, it contains a non-linear integral operator and is cumbersome to work with in many cases of interest. Furthermore, it does not easily lend itself to the generation of succinct fluid models. To address this issue, we recently developed [19] a relativistically covariant extension of the non-relativistic Lenard-Bernstein equation and used it to generate a new relativistic plasma fluid model that includes dissipative effects. Our induced fluid model contains new terms that arise from the non-trivial geometry of the unit hyperboloid in 4-dimensional (Lorentzian) phase space, and was used to investigate electric waves.

For small amplitude classical electromagnetic fields recourse is often made to a linear approximation scheme in which the appropriate constitutive relations arising from the coupled matter-field equations are linearized. If the medium is uniform

in space Fourier techniques are adequate since (if gravity is ignorable) the coupled system can be projected into plane-wave eigen-solutions of the Helmholtz equation. Such an approach leads to the concept of classical dispersion in which the parameters describing such eigen-solutions are required to satisfy constraints involving properties of the medium. However if the medium is inhomogeneous, exhibits relaxation or memory properties, or gravitational fields are present such Fourier methods no longer diagonalize the system and prove impractical. We have developed new approaches to circumvent these difficulties [20] and obtained integral equations that supercede classical dispersion relations in homogeneous media permitting investigation of Landau damping in non-stationary and inhomogeneous relativistic plasmas.

Finally, we have initiated investigation of the interaction of electromagnetic fields with accelerating matter by exploring constitutive relations for uniformly rotating media [21-23] and exploring how forces and torques can be defined covariantly and calculated for arbitrarily moving media. In particular, for a class of media with simple electromagnetic constitutive properties we show that, under the influence of an incident monochromatic, circularly polarized, plane electromagnetic wave, the Abraham and symmetrized Minkowski tensors induce different time-averaged torques on a uniformly rotating materially inhomogeneous dielectric cylinder and suggest that this observation may offer new avenues to explore experimentally the covariant electrodynamics of more general accelerating media.

In summary, work over the past twelve months in the Lancaster Mathematical Physics Group and Cockcroft Institute has led to a number of new avenues for exploring the behaviour of intense laser-plasmas.

Acknowledgements

References

1. M Marklund, Nat. Photonics **4** (2010) 4

2. J. Schwinger, Phys. Rev. **82** (1951) 664

3. M. Born and L. Infeld, Proc. R. Soc. Lond. A **144** (1934) 425

4. G.W. Gibbons and C.A.R. Herdeiro, Phys. Rev. D **63** (2001) 064006

5. R. Ferraro, Phys. Rev. Lett. **99** (2007) 230401

6. T. Dereli and R.W. Tucker, Euro. Phys. Lett. **89** (2010) 20009

7. D.A. Burton, R.M.G.M. Trines, T.J. Walton and H. Wen, "Exploring Born-Infeld electrodynamics using plasmas", arXiv:1006.2246

8. G. Boillat, J. Math. Phys. **11** (1970) 941

9. J. Plebanski, Lectures on Non-Linear Electrodynamics, (Nordita, Copenhagen, 1970)

10. E.S. Fradkin and A.A. Tseytlin, Phys. Lett. B **163** (1985) 123

11. P.A.M. Dirac, Proc. R. Soc. Lond. A **167** (1938) 148

12. A.I. Akhiezer and R.V. Polovin, Sov. Phys. JETP **3** (1956) 696

13. J.M. Dawson, Phys. Rev. **113** 383 (1959)

14. D.A. Burton and A. Noble, J. Phys. A: Math. Theor. **43** (2010) 075502

15. R. Gallego Torrome, "Averaged dynamics associated with the Lorentz force equation", arXiv:0905.2060

16. R. Gallego Torrome, "Averaged Lorentz dynamics and an application in plasma dynamics", arXiv:0912.0183

17. R. Gallego Torrome, "Fluid models from kinetic models using a geometric averaging procedure", arXiv:0912.2767

18. J. Gratus, "Distributional solutions to the Maxwell-Vlasov equations", arXiv:0809.2944

19. A. Noble and D.A. Burton, "Modelling collisions in a relativistic plasma", arXiv:0910.4368

20. J. Gratus and R.W. Tucker, "Covariant constitutive relations, Landau damping and non-stationary inhomogeneous plasmas", arXiv:1003.2062

21. C.E.S. Canovan and R.W. Tucker, "Maxwell's equations in a uniformly rotating dielectric medium and the Wilson-Wilson experiment", Am. J. Phys. (accepted)

22. S. Goto, R.W. Tucker and T.J. Walton, "The electrodynamics of inhomogeneous rotating media and the Abraham and Minkowski tensors. I. Basic Theory", Proc. Roy. Soc. A (accepted). arXiv:1003.1637

23. S. Goto, R.W. Tucker and T.J. Walton, "The Electrodynamics of Inhomogeneous Rotating Media and the Abraham and Minkowski Tensors II: Applications", Proc. Roy. Soc. A (accepted). arXiv:1003.1642

Cavitation and Shock Wave Formation in Dense Plasmas by Relativistic Electron Beams

Contact *iab500@york.ac.uk*

I. Bush and J. Pasley

Department of Physics, University of York, Heslington, York, YO10 5DD, UK

A. P. L. Robinson

Central Laser Facilty, STFC Rutherford Appleton Laboratory, HSIC, Didcot, Oxon, OX11 0QX, UK

R. J. Kingham

Blackett Laboratory, Imperial College London, London, SW7 2BZ, UK

Introduction

Fast-ignition is an inertial confinement fusion scheme [1,2] where a separate igniter laser pulse is fired into a compressed capsule of deuterium-tritium fuel. This creates a beam of hot electrons which heat the compressed fuel close to the centre.

Once a high enough temperature is reached a self-sustaining burn-wave can propagate through the rest of the cold fuel and heat it up to fusion temperatures. The original fast-ignition scheme envisaged achieving this by using the igniter laser to bore up to the critical density in a plasma, where a beam of hot electrons would be produced that would heat the central area in the fuel [3]. Recently there has been more interest in cone-guided fast-ignition, where a hollow gold cone is embedded in the initial capsule, creating a clear path for the laser energy to reach the centre of the fuel [4, 5]. In either variant the propagation of a relativistic electron beam is a critical element.

A relativistic electron beam propagating through a background plasma will set-up a charge balancing resistive return current, such that

$$\mathbf{j}_f + \mathbf{j}r \simeq 0$$

where j_f and j_r are the forward going fast electron current and the return current respectively. A resistive electric field is formed such that $\mathbf{E} = -\eta\mathbf{j}_r = \eta\mathbf{j}_f$, where η is the resistivity of the plasma [6, 7]. This resistive return current will create a $\mathbf{j}_r \times \mathbf{B}$ force on the plasma and a pressure gradient via Ohmic heating, both of which would be expected to push the plasma away from the centre of the electron beam. 2D-3V Vlasov-Fokker-Planck simulations of this effect have previously be done by Kingham *et al.* [8], which showed collimation of the electron beam. A similar problem applied to cosmic rays passing through low density plasma has been looked at by Bell [9].

In this work we used a simple analytic model which predicts the density, pressure, magnetic field and velocity in the plasma to study the basics of cavitation in these circumstances. This model will be used to explore the strength of the cavitation over a wide range of parameter space that is of interest to fast-ignition fusion. Using an MHD code created specifically to look at this problem the analytic model will be shown to be effective at predicting the amount of cavitation that will occur in a plasma. From both the analytic model and the full numerical simulation it is clear that the effect of the pressure gradient caused by Ohmic heating is dominant in the cavitation process. The region of hot electron current density and mass density can also be found where the pressure gradient from the Ohmic heating is so extreme that a shock wave can be launched into the surrounding plasma.

Theory

To understand what happens to the background plasma the collisionless fast electron current and resistive return current need to be added to the MHD equations. For Ampère's law we make a hybrid approximation of the form

$$\nabla \times \mathbf{B} = \mu_0(\mathbf{j}_f + \mathbf{j}_r) \simeq 0$$

with the displacement current neglected. We also use an Ohm's Law of the form

$$\mathbf{E} + \mathbf{v} \times \mathbf{B} = -\eta\mathbf{j}_r$$

where there is a contribution to the electric field due to the resistive return current.

In addition the return current will cause Ohmic heating in the plasma

$$\frac{\partial T}{\partial t} = \frac{\gamma - 1}{n_i k_B} \eta j_r^2$$

where n_i is the number density of ions in the plasma, such that $n_i = \rho/m_i$, k_B is Boltzmann's constant and $\gamma = C_p/C_v$ is the adiabatic index. Throughout this work thermal conductivity is neglected.

Spitzer resistivity is used, which is given by

$$\eta(T) = 10^{-4} \frac{Z \ln \Lambda}{T_{eV}^{3/2}}$$

where Z is the ionic charge, $\ln \Lambda$ the Coulomb logarithm and T_{eV} the temperature of the background plasma in eV. This is valid for temperatures in the plasma above 100 eV at solid density, and is valid at lower temperature for lower mass densities. A fixed ionisation state is assumed. The return current is modelled as a rigid beam in 1D, with a Gaussian profile such that

$$j_r(x) = -j_f(x) = j_0 e^{-x^2/2R^2}$$

where R determines the radius of the electron beam.

These equations for the effects caused by the return current can be added into the MHD equations which describe the evolution of the plasma.

Although these equations are not able to be solved exactly analytically, by neglecting the adevction terms in the resulting equations for the density, pressure, velocity and magnetic field we can obtain approximations for these parameters in the plasma, as a function of time and space. This allows us to take a parameter scan across the different values of hot electron current density and initial mass density to find the regimes where plasma cavitation is likely to be significant.

An example of the density profile in a hole boring fast-ignition scenario can be found in figure 3a of [10]. This shows that the fast electrons that are produced at the critical surface will have to cross a range of densities from 10 kg m^{-3} up to 10^6 kg m^{-3}. For much of this distance, hundreds of microns, the density is in the range 50 - 1000 kg m^{-3}. When comparing this range to figure 1 it can be seen that the cavitation effect will be significant over much of the distance the fast electrons are propagating over.
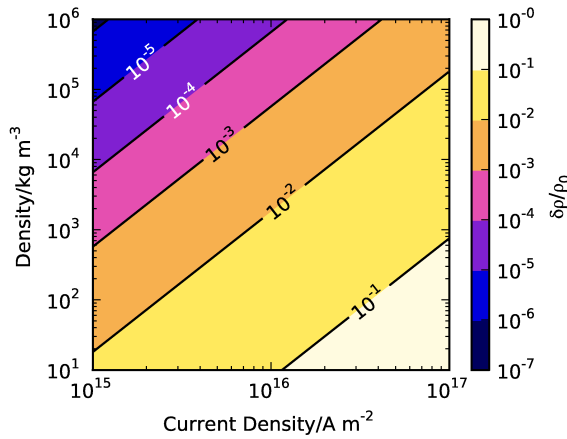
Figure 1. A parameter scan across density and current from the model. The initial parameters are $T_0 = 100$ eV, $R = 3$ μm, $Z = 1$ and $\ln \Lambda = 10$, and the final time is $t = 3$ ps. The contour lines show increases of a factor of 10.

A similar treatment can be applied to find the parameters for which shocks are expected to form in the plasma. We have been able to obtain a formula for the velocity in the plasma from the MHD equations so it can be determined when $v_{max} > c_s$, where c_s is the sound speed in the plasma.

Figure 2 shows a parameter scan across the same values as in figure 1. The colour scale shows the time at which a shock would form in the plasma, which is at an initial temperature of 100 eV. At the top end of the colour scale times are ≥ 20 ps, meaning that no shock would be formed within 20 ps. The region in which the shock would be formed in 10 - 20 ps is very narrow, as the transition is being made into the region where a shock would never form.
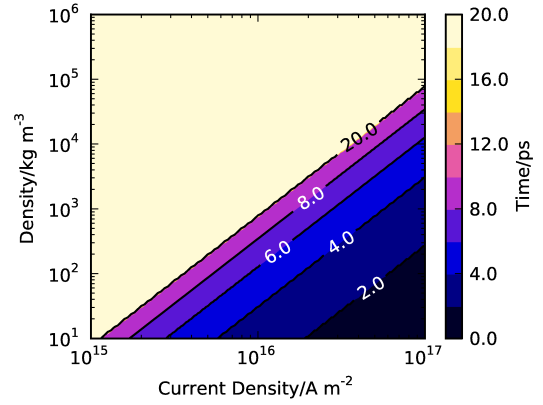
Figure 2. The time taken for shocks to form for different values of current density and mass density. The initial parameters are the same as in figure 1. Above the 20 ps contour the plot is saturated, so a shock would take more than 20 ps to form, if it would ever form.

Code Description

The 1D MHD code that was developed was based on the method by Ziegler described in [11]. This solves the MHD equations with the additional terms that arise due to the hot electron current.

The fast electron current is added into the code via the return current given in the previous section. Spitzer resistivity is used, along with the resistive magnetic field growth and Ohmic heating terms

As the problem here is only one dimensional some of the more sophisticated parts of the code, like the enforcement of $\nabla \cdot \mathbf{B} = 0$, are not required. Otherwise the implementation used here is as described by Ziegler, with RK2 integration of the MHD equations. Numerical diffusion is low due to the method of interpolation onto the cell walls, and open boundary conditions are used. The code was verified against the results of figure 3b in [12].

Results and Discussion

To begin with we will look at a typical case of interest to fast-ignition and compare the results from the code with the results predicted by the analytic model. In figure 3 the results are compared for the case where $j_0 = 10^{16}$ A m^{-2} and $\rho_0 = 100$ kg m^{-3}.

From figure 3 it can be seen that the analytic model and the MHD code give very good agreement. For the density the analytic solution over-estimates the cavitation in the central region, and underestimates it towards the edges. This can be understood by the lack of advection from the central region in the analytic model. The analytic prediction for the magnetic field is extremely close to the full numerical solution.

The plot for the velocity shows that the pressure gradient term alone gives a reasonable estimate of the velocity in the plasma. If a more complete consideration is used, including the $\mathbf{j}_r \times \mathbf{B}$ force, then the velocity becomes slightly underestimated in the regions where it is overestimated and vice-versa.
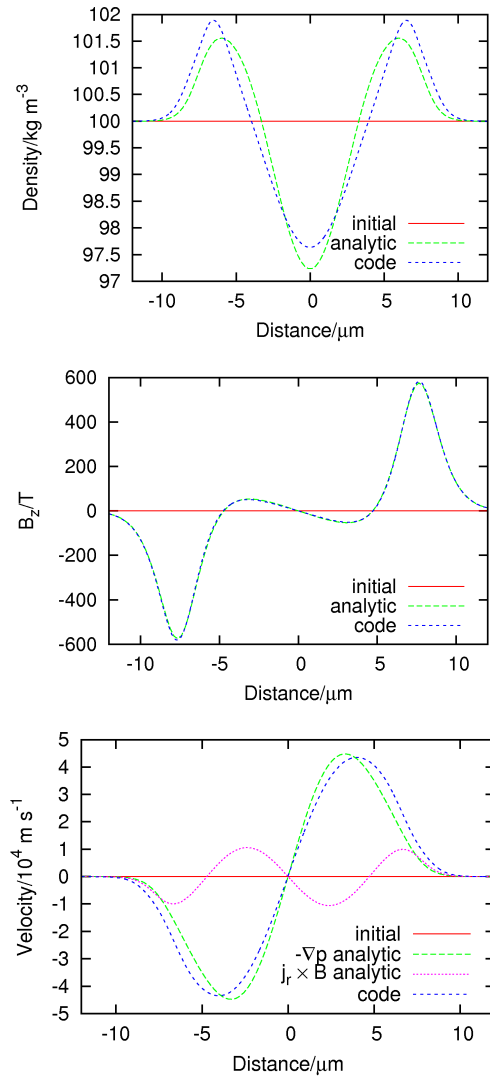
Figure 3. Plots of the density, magnetic field and velocity after 3 ps for $j_0 = 10^{16}$ A m^{-2} and $\rho_0 = 100$ kg m^{-3}. Otherwise the same values are used as in figure 1. In the plot for velocity the analytic contribution from the pressure gradient and $j \times B$ force are shown separately, demonstrating the dominance of the pressure gradient.

If the return current is driven for long enough at a high enough current density and low enough mass density shocks can form in the plasma. In figure 4 an example is shown for a return current of 10^{17} A m^{-2} and a mass density of 10 kg m^{-3}. At 5 ps the beginning of the shock formation can be seen and by 11 ps a sharp shock front has been formed. Because of the extreme amount of cavitation in this situation the analytic model can not be expected to give sensible results here.

From figure 4 it can be seen that we have essentially been able to produce a blast wave in this case. This is not unexpected, as we have rapidly put a lot of energy into a small volume. It should be noted that figure 2 shows only the time taken for $v_{max} > c_s$, and not the time for a well defined shock to form, as is only seen between 5 and 11 ps in figure 4. Not included in the MHD code is the effect of radiative heating, in this regime it will certainly have an effect on the form of the shock front obtained.
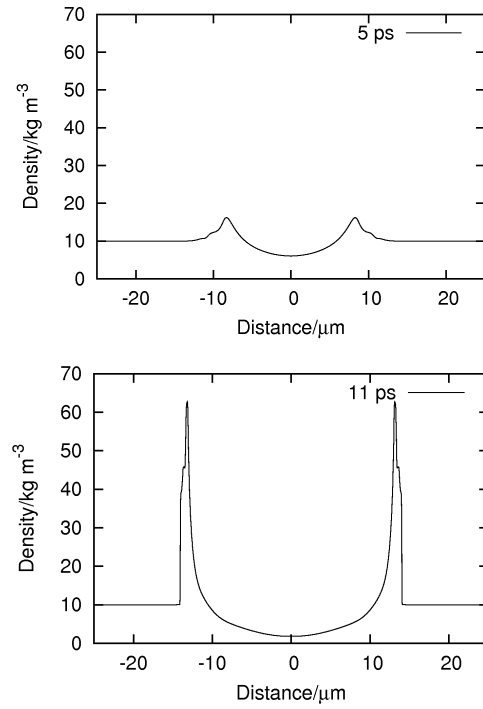
Figure 4. Density plots from the MHD code showing shock formation caused by the resistive return current. The initial parameters in this case were $j_0 = 10^{17}$ A m^{-2} and $\rho_0 = 10$ kg m^{-3}, other parameters were the same as for the results shown in figure 3.

Conclusions

It has been shown that for parameters of interest to fast-ignition the cavitation effect can be quite significant, getting up to 10% of the initial density after just 3 ps. The good agreement between analytic theory and fully non-linear MHD simulations indicates that one can be confident that cavitation is relevant to fast-ignition. Similarly shocks can be formed in fast-ignition relevant plasmas after just a few ps. These were predicted by the analytic model and an example from the MHD code has been shown.

References

1. Nuckolls J *et al*. 1972 Nature **239** 139

2. Lindl J 1995 Phys. Plasmas **2** 3933

3. Tabak M *et al*. 1994 Phys. Plasmas **1** 1626

4. Tabak M *et al*. 1997 Lawrence Livermore National Laboratory patent disclosure, IL8826B

5. Kodama R *et al*. 2001 Nature **412** 798

6. Glinsky M E 1995 Phys. Plasmas **2** 2796

7. Davies J R *et al*. 1997 Phys. Rev. E **56** 7193

8. Kingham R J *et al*. (accepted) 6th Inertial Fusion Sciences & Applications conference

9. Bell A R 2005 Mon. Not. R. Astron. Soc. **358** 181

10. Tabak M *et al*. 2005 Phys. Plasmas **12** 057305

11. Ziegler U 2004 J. Comp. Phys. **196** 393

12. Ryu D and Jones T W 1995 Astrophys. J. **442** 228

Alpha-particle stopping power for dense hydrogen plasmas

Contact *D.J.Edie@warwick.ac.uk*

D.J. Edie, J. Vorberger and D.O. Gericke

Centre for Fusion, Space and Astrophysics,
Department of Physics, University of Warwick,
Coventry, CV4 7AL, UK

Introduction

With the completion of the NIF facility, inertial confinement fusion (ICF) has made considerable advances and can now be considered as a promising method for an energy source for the future [1,2]. Achieving ICF involves the creation of a dense, high temperature plasma. The way in which charged particles pass through such plasmas and deposit their energy is of interest to ICF research for two primary reasons. The first case is in the simulation of ion beams as primary drivers in ICF [3]. In this case, knowledge of the distribution of the beam energy across the target is important in order to reduce the probability of instabilities arising.

The second case is the modeling of the α-particle heating experienced by dense plasmas surrounding the hot spot where fusion reactions are already taking place. Immediately after the initial, externally driven, compression stage during ICF experiments, sufficient temperature and density conditions for fusion [4] are created at the centre of the fuel capsule. The fusion reactions that occur create α-particles that deposit their kinetic energy in the surrounding plasma and heat a part of the outer highly compressed plasma to fusion temperatures. As a result more α-particles are created from new fusion reactions. This dependent chain of fusion reactions and further heating is a burn wave that needs to propagate from the centre of the fuel outwards through the whole capsule, to allow for efficient, high gain targets. Thus, the energy deposition in high-density hydrogen is important to describe the creation of a burn wave and, thus, modeling conditions for high gain targets.

To simulate the energy deposition process, we calculate the stopping power as a rate of kinetic energy lost by an incident particle per unit distance traveled through the stopping medium, $-dE/dx$. Numerically integrating this quantity along the beam path will yield the energy deposition profile of the α-particles. Different beam profiles can easily be generated by weighted distributions of initial energies.

In this work, we combine advanced kinetic models for the beam-plasma interactions [5.6] with state of the art descriptions of the target plasma. The latter consists of dense hydrogen and is described by full quantum simulations (DFT-MD) [7-10]. A one-dimensional density line profile is then calculated by taking the density along a line through the simulation box at an oblique angle. This profile is used as a dynamic input parameter for the calculation of the energy loss of α-particles with an energy of 3.5 MeV passing through this plasma.

Many existing models currently describe the stopping power experienced by ions in a variety of target mediums. Dense plasma effects such as quantum degeneracy, self-energy, ionisation and dynamical screening are not taken into account in more classical stopping models [11,12]. Accuracy of existing models can be improved upon by recalculating the stopping power using a quantum mechanical description of the system and the creation of High Energy Density (HED) states of matter allows experimentation in new regimes of matter where models incorporating these effects can be tested.

DFT-MD Simulations for the Target

The density profile of the hydrogen target is calculated through quantum density functional molecular dynamics (DFT-MD) simulations using the simulation package VASP [8-10]. From an initial density, a bcc crystal structure of hydrogen nuclei is produced. The number of ions necessary to form the periodic DFT system is determined by the particular crystal structure used and the spatial size of the system is determined by the initial density. These ions are then given an initial Maxwellian thermal velocity distribution. The electrons are initialized, often as atomic orbitals.

From this converged electronic configuration, in the external field of the ions, new forces on the ions can be calculated. With these, a molecular dynamics step of the ions is performed. The resulting new ion configuration gives rise to a new solution of the Kohn-Sham equations governing the electron configurations and, thus giving a new electronic density configuration. This can be used to implement the next MD step.

The exchange correlation functional, describing electron interactions, is the major ingredient of the DFT step for the electrons. It modifies the potential felt by the electrons due to the many-body interactions and Pauli blocking. As this potential depends on the electron configuration, convergence must be reached between the new electron wave functions and the exchange correlation functional. Throughout the simulation the ion temperature is kept constant using a Nose-Hoover thermostat and the iterative DFT-MD process is repeated until the lowest free energy of the electrons is reached (see Ref. 13).

Using this method, a periodic three-dimensional density profile is formed, which includes both the locations of the nuclei and the electron density at cubic grid points. Then we start from a random footpoint in the DFT box and follow a path whose direction is set by random angles of azimuth and inclination. In this way, a one-dimensional line density can be extracted. To calculate the density at a generalized co-ordinate a trilinear interpolation scheme is applied to the densities at the eight neighboring grid points of the box. The profile is evaluated at 0.1 Angstrom increments along the described path. Fig. 1 shows an example of a line profile obtained by this procedure.
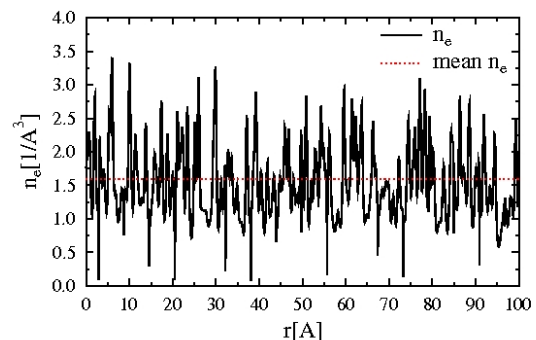

Fig. 1: Line density profile segment taken from a DFT-MD simulation for dense hydrogen with T=10000K and $n_e= 1.661\times10^{24}cm^{-3}$.

Quantum Calculations of Stopping Power

The stopping power experienced by a charged particle traveling through a plasma, which is due to elastic binary collisions, can be calculated by the following expression which follows from the quantum Boltzmann equations [14,5].

$$\frac{\partial}{\partial t}\langle E\rangle_{T-Matrix} = \frac{1}{(2\pi)^3 \hbar^3}\sum_c \frac{m_e^2}{m_{ce}^3}\frac{n_e \Lambda_e^3}{v}k_B T \int_0^\infty dp\, p^3\, Q_{ce}^T(p)$$

$$\times\left\{\left(1 - \frac{m_{ce}k_B T}{m_e p^2}\right)\exp\left[-\frac{m_e}{2k_B T}\left(\frac{p}{m_{ce}} - v\right)^2\right]\right.$$

$$\left.+\left(1 + \frac{m_{ce}k_B T}{m_e p^2}\right)\exp\left[-\frac{m_e}{2k_B T}\left(\frac{p}{m_{ce}} + v\right)^2\right]\right\}.$$

The evaluation of this expression requires the momentum transfer cross section for electron-ion scattering Q^T. This cross section can be determined from phase shift analysis of the electron wave functions [15], which are dependent on the potential through which the incident beam is scattering. Here, we use a Debye potential to take screening into account. The complex scattering for a charged particle passing through a large composite body is here reduced to multiple two-body scattering events.

To calculate the phase shift the Numerov algorithm [16] is employed to solve the radial Schrödinger equation,

$$\left(\frac{\partial^2}{\partial r^2} + E - V(r) - \frac{l(l+1)}{r^2}\right)R(r) = 0$$

The phase shift of a scattering state is the measured difference in phase between the wave function as calculated in the potential, $V(r)$, and the wavefunction as calculated for free electrons. Phase shift analysis [15] of scattering states, over all available linear and angular momentum values, allows calculation of the momentum transport cross section via [13]

$$Q^T = \frac{4\pi}{k^2}\sum_{l=0}^\infty (l+1)\sin^2(\delta_l(k) - \delta_{l+1}(k))$$

Stopping power in binary collision approximation can then be calculated by substituting the calculated momentum transport cross sections into the Boltzmann expression. Dynamic screening effects can be modeled by using a velocity-dependent screening length [5,6], which also accounts for the excitation of collective modes (plasmons). For this work, the fit proposed in Ref. 10 has been employed in order to reduce the computational intensity of calculating this stopping power.

Energy Loss Comparisons

A solver has been written which takes inputs of temperature and density, calculates the stopping power and simulates the energy loss of an α-particle as it passes along a one-dimensional path.

Bragg curves, stopping power versus stopping path length, are calculated by the solver for 3.5 MeV α-particles. These curves are compared for the cases of stopping calculated using the DFT-MD density profile and for stopping power calculated using the mean density of the three-dimensional dense hydrogen DFT-MD simulation box.
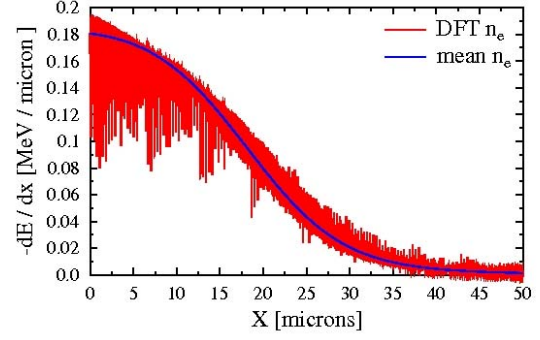

Fig. 2: Comparison of α-particle stopping in hydrogen using a density profile obtained by DFT-MD and a constant mean density. The beam energy is E = 3.5MeV. The plasma has a temperature of T=10000K and a mean electron density of $n_e = 1.661\times10^{24}$ cm^{-3}.

Despite the frequent large fluctuations in the density profile, causing large fluctuations in the calculated values of stopping power, there is good agreement between the general functional form of the Bragg curves for the two cases and also between the ion ranges calculated in the two cases. This implies that, for a beam path length much greater than the width of the DFT profile, the energy deposition profile of the incident particles can be well approximated by calculations that use the average target density. However, the straggling of the beam is strongly underestimated by considering a constant mean density as the quantum simulations show huge microscopic fluctuations that are fully reflected in the Bragg curves.
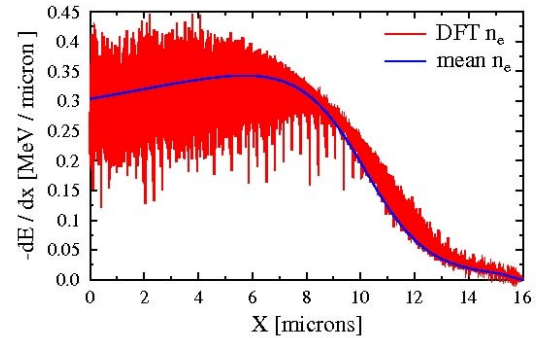

Fig. 3: As Fig. 2, but for a temperature of T=20000K.

Range Comparisons

The ion range is the distance at which all of the kinetic energy of the ion has been deposited in the stopping medium. Actually, the ion is not fully stopped at this point, but thermalized to the plasma ions. The depth of this point into the stopping medium is obviously highly dependent on the initial kinetic energy of the incident particle and the plasma conditions.

For a well-defined analytical solution for the stopping power, the range can be calculated from the integral

$$Range = \int_{E_0}^0 \left(\frac{dE}{dx}\right)^{-1} dE.$$

However, the ranges have been calculated in this work using the stopping solver to integrate along the beam path until the step at which $E_b \leq 0$, where E_b is the spatially dependent energy of the beam particles.
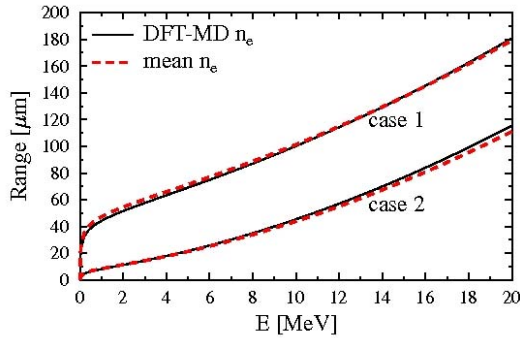
Range of α-particles in dense hydrogen using the highly fluctuating electron density from DFT-MD simulations (see Fig. 1) and a constant mean density. See Figs. 2 and 3 for the plasma conditions (in particular the temperatures) of cases 1 and 2, respectively.

The α-particle ranges are calculated, at initial kinetic energies from zero to 20 MeV for both mean and fluctuating electron density from DFT-MD. For the case of the beam velocity being less than the electron thermal velocity in the target medium, the stopping power can be approximated as a linear frictional force, $-dE/dx = R v_b$. Solving for the analytical solution to the range in the low energy approximation shows good agreement with the numerical calculations. In the high velocity case, the Bethe limit can be employed and the stopping power is approximated by $-dE/dx = c/v^2$. It is also found that analytical solutions of the range solved from this form of stopping power show good agreement to the ion ranges calculated by the numerical solver. The comparison in Fig. 3 demonstrates that the range of the α-particles can be calculated from mean densities as the large fluctuations in the density cancel during the stopping paths. Thus, the predicted size of the hot spot needed in ICF targets is mainly determined by the physics included in the stopping power model employed. More advanced models [5,6,18,19] should receive more attention although they are numerically difficult to implement into a hydrodynamic simulation.

Conclusions

For beam energies from 0–20 MeV, a good agreement is obtained between calculated ion ranges for α-particles stopping in dense hydrogen for both highly fluctuating electron densities from DFT-MD and uniform averaged density profiles. In addition, the range calculations demonstrate good agreement with analytical range calculations using stopping power approximations in the limit of both the high and low kinetic energy as well.

This agreement implies that for calculations of large-scale effects, such as ion range or averaged energy deposition, the increased accuracy provided by applying a DFT-MD density profile has little effect on the final result. It is also observed that the general functional form of the Bragg curves calculated for the variable and uniform density cases is similar. However, in variable density DFT-MD cases, fluctuations in density cause dramatic changes in the calculated stopping power over small spatial scales. This huge straggling must be considered in situations with small fluxes where heating cannot be averaged over many particles.

References

1. S.H. Glenzer *et al.*, Science **327**, 1228 (2010).

2. J. Lindl, Phys. Plasmas **2**, 3933 (1995).

3. B.G. Logan, L.J. Perkins and J.J. Barnard, Phys. Plasmas **15**, 072701 (2008).

4. J. D. Lawson, Proceedings of the Physical Society B **70**, 6 (1957).

5. D.O. Gericke and M. Schlanges, Phys. Rev. E **60**, 904 (1999).

6. D.O. Gericke, Laser and Particle Beams, **20**, (2002).

7. K. Wünsch, J. Vorberger and D. O. Gericke, Phys. Rev. E **79**, 010201(R) (2009).

8. G. Kresse and J. Hafner, Phys. Rev. B **47**, 558 (1993).

9. G. Kresse and J. Hafner, Phys. Rev. B **49**, 14251 (1994).

10. G. Kresse and J. Furthmüller, Phys. Rev. B **54**, 11169 (1996).

11. H. Bethe, Ann. Phys. **5**, 325-400, (1930).

12. C.-K. Li and R.D. Petrasso, Phys. Rev. Lett. 70, 3059 (1993).

13. J.Vorberger, I. Tamblyn, B. Militzer, and S. A. Bonev, Phys. Rev. B **75**, 024206 (2007).

14. W.D. Kraeft and B. Strege, Physica A **149**, 313 (1988).

15. Roger G. Newton, *Scattering Theory of Waves and Particles* (Dover Publications, 2002).

16. B.V. Numerov, Mon. Not. R . Astron. Soc. **84**, 592, (1924).

17. H.A. Gould and H.E. DeWitt, Phys. Rev. **155**, 68-74 (1967).

18. D.O. Gericke, M. Schlanges & Th. Bornath, Phys. Rev. E **65**, 036406 (2002).

19. G. Zwicknagel, C. Toeppfer, and P.-G. Reinhard, Phys. Rep. **309**, 117 (1999).

An Object-Oriented 3-D View-factor Code for Hohlraum Modelling

Contact *jp557@york.ac.uk*

M. J. Fisher[1], J. Pasley[1,2]

[1]*Department of Physics, University of York Heslington, York, YO10 5DD, U.K.*

[2]*Central Laser Facility, STFC Rutherford Appleton Laboratory Chilton, Didcot, Oxon., OX11 0QX, U.K.*

Introduction

The design of the hohlraum plays a crucial role in indirect-drive ICF. Both the hohlraum geometry itself and the configuration of incident drive lasers are major factors in determining whether an experiment will be successful. Alteration of these factors will alter both the driver-capsule coupling efficiency and the uniformity of implosion of the fuel capsule. Analytic approaches can be utilized to give a theoretical insight into these effects, but often require limiting simplifications such as a spherical hohlraum[1]. Alternatively, a numerical approach can be used to obtain a more realistic model of the system.

A radiation hydrodynamics simulation would deliver the best predictive results in this situation. While accounting for physical processes on a fine level of granularity, these calculations can be prohibitively computationally expensive; especially if performed in three dimensions. In addition, models can be difficult and time consuming to correctly set up. Less complex are view-factor methods. These allow a whole hohlraum to be modelled relatively inexpensively, although low level details (such as driver-wall coupling) must be parameterised rather than calculated *ab initio*[2].

View-factor based hohlraum modelling codes use simple geometric arguments to determine the quantities of radiation that can flow to one part of a hohlraum geometry from another, and then solve a power balance equation to calculate the spatial distribution of radiation throughout a target[3]. Because of the relative speed involved in setting up and running simulations, 3D view-factor codes are especially suited to prototyping experimental target designs.

While very useful for experiment design, existing commercial codes can be costly and may also represent a "black box" since source code may not be provided. Thus, we created a new, easy to use 3D view-factor code that can be employed to study radiation effects in a wide range of hohlraum geometries. It can be used to easily create hohlraum geometries from a number of geometric primitives. Drive laser configurations can be specified, and are implemented via a ray-tracing algorithm. Given a pulse shape, the code can then calculate the time-dependent evolution of the radiation distribution throughout the hohlraum. As well as raw data output, visualisation tools have been created to display the resulting data as a 3D false colour animation.

Mesh Generation

For numerical techniques to be applied, a hohlraum model must be discretised into a mesh of triangular faces. Triangles as a basis for mesh construction are preferred for a number of reasons. The first is that triangle vertices are guaranteed to be co-planar – a triangle's normal cannot vary over the face. This is important as face normals are used heavily in the calculation of the view-factors. Second, simple and efficient tests exist for an intersection between a line and a triangle, which aids computation speed when implementing ray-tracing and occlusion detection algorithms. To simplify calculation, faces have normals in one direction only; they are effectively transparent from the back.

The user can construct hohlraums by combining cylinders, disks, annular rings and spheres. The dimensions of these objects, their orientations and positions are specified in an XML configuration file. As an aid to the process, a designer application is included that allows the user to generate the configuration files in a more user friendly manner. As well as being capable of creating and editing the properties of various primitives, the resulting mesh can be viewed and rotated in a 3D preview window (See fig.1).

The *meshGenerator* program takes a configuration file created by the designer as a command line argument, and writes a binary file containing the face data. This file can be used as input to the other programs in the code, and contains the positions, areas and normals of each face.
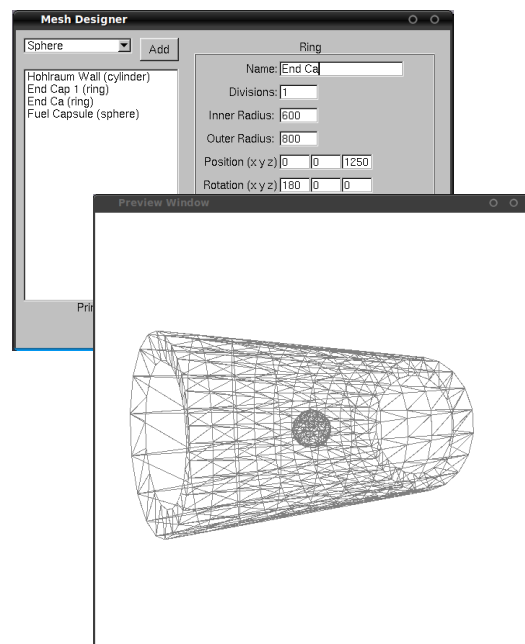

Figure 1 – The mesh designer application is a graphical interface that allows the user to easily create model configuration files for the code by interactively editing properties of 3D primitives.
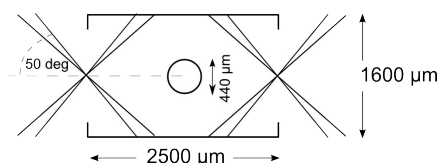

Figure 2 – The dimensions of the hohlraum used in the HEP-1/ Precision Nova experiments at LLNL [8]. This series of experiments were numerically modelled to determine if the code could successfully reproduce experimental results

View-factor Calculation

Once all geometric details of the mesh have been calculated, the possible ways in which radiation can flow from one face to another may be evaluated. This is accomplished by means of a 2D view-factor matrix. The view-factor between two faces F_{ij} is the fraction of total energy that leaves face i and arrives at face j. This is given exactly by the view-factor integral[4]:

$$F_{ij} = \frac{1}{2 \pi A_i} \int_{A_i} \int_{A_j} \frac{\cos \theta_i \cos \theta_j}{\pi S^2} dA_i \, dA_j$$

Where A_i and A_j are the areas of faces i and j, S is the distance between the differential area elements, and θ_i and θ_j are the angles between the normals of the respective elements. In the limiting case of a large number of small, co-planar faces this equation can be simplified to

$$F_{ij} = \frac{1}{\pi A_i} \frac{A_i A_j}{S^4} (\hat{n}_i \cdot \vec{r})(-\hat{n}_j \cdot \vec{r})$$

Where $\hat{n}_i$ and $\hat{n}_j$ are the normal vectors of faces i and j respectively, and $\vec{r}$ is the vector from face i to face j. The reciprocity relation $A_i F_{ij} = A_j F_{ji}$ saves us from having to calculate the entire matrix; once F_{ij} is known F_{ji} can be trivially calculated.

The calculation is complicated by the possibility of a view-factor being totally or partially occluded by another face. In this implementation, we assume if the vector between the centre of two faces intersects any other face in the mesh, the view-factor between those faces becomes zero. This becomes a more accurate approximation as mesh resolution is increased, but at the same time introduces a significant computational overhead. If required for every face in the mesh, the complexity class of this algorithm becomes $\sim O(N^3)$ for N faces; as such the calculation of this matrix is generally the most time consuming part of the computation. The view-factor matrix is generated in this code by the *viewFactorCalc* program, which takes a mesh file as its input, and writes out a file containing the view-factor matrix.

The implementation of the view-factor calculation in this code was tested by comparing its results to analytically known solutions. A classic example is the view-factor between two circular parallel plates. Analytically, the view-factor between two parallel circular plates of radius 1000μm with a separation of 1500μm is 0.25 [5]. With a plate mesh surface resolution of 802.1 mm⁻², the numerical error was 4.6 parts per million – a small error within manageably low resolutions.

Beam Ray-tracing

A ray-tracing algorithm was used to allow a realistic representation of a set of lasers. A laser can be described by a focal point, a direction vector, and an F-number. Once these quantities are known, the beam can be approximated by a large set of evenly spaced rays, each carrying an evenly distributed fraction of the beam's total power. The power of the ray is then applied to the intersecting face closest to the laser source. In this initial version of the code, the coupling between beam and surface is assumed here to be perfect – all the power from each ray is re-emitted diffusely by the face it is incident upon. This is a fair approximation, despite the complex physics involved in the x-ray generation process: depending on the target design, a large fraction of incident energy can be converted to x-rays[6].

In order for this to produce realistic results, the number of rays in each beam must be such that many rays fall on each face. This is achieved by automatically increasing the density of rays in each beam until the average number of rays intersecting with a face is at least ten. This ensures a smooth and realistic distribution of beam power on arbitrary resolution geometries.

Drive beam configurations are also specified in an XML configuration file, along with a few other simulation parameters. As well as creating individual beams, the user can also easily create rings of beams by additionally describing the number of beams in each ring and their angle to a direction vector.

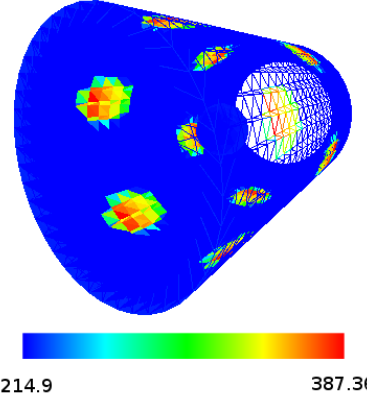**Solving the Radiosity Equation**

Figure 3 - Numerically calculated distribution of radiation temperature in eV over the surface of the HEP-1 target. This image was taken from the 3D viewer developed for use with the code.

In order to calculate the static power balance condition throughout a hohlraum mesh, one can consider the radiosity equation, which must be true in a steady state[7]:

$$B_i - \alpha_i \sum_i F_{ij} B_j = E_i$$

Where B_i, B_j are the radiosities of faces i and j, α_i is the albedo of face i, and E_i is any external power contribution to face i – e.g. power delivered from a laser. The radiosity of a face is the power it emits per unit area. By Stefan-Boltzmann law, it may be expressed as $B_i = \sigma T_i^4$, where T_i is the face temperature and σ is the Stefan-Boltzmann constant. The radiosity equation is an expression of the fact that in a steady state, the power leaving a face must be equal to the power incident on the face. The only unknown parameter in this equation is the albedo; here it is simplified to a constant scalar value. Later it will be seen that this is a reasonable approximation.

Using matrix inversion methods exact solutions to this equation can be found, but this can be computationally expensive; additionally, for most cases exact solutions are not required. In this code, a Jacobi iteration is used to converge upon the solution. Once a user defined minimum percentage difference between old and new radiosity values has been met, the solution is deemed good enough and the process terminates. The final level of convergence can also be used to estimate the error in the numerical result.

The radiation transport code was tested by comparing its numerical results to experimentally observed hohlraum temperatures. The Nova laser at Lawrence Livermore National Laboratory conducted widely-documented experiments with various hohlraum geometries, dummy capsules and laser powers[8]. Here, the HEP-1/Precision Nova series of experiments were selected for modelling - the dimensions of the hohlraum used can be seen in fig 2.

A suitable XML configuration file to describe the experiment's hohlraum was created and used as input to the *meshGenerator* program. The view-factors were then calculated. This particular experiment utilises two beam cones at an incident angle of 50 degrees to the axis – each has five beams, and the peak power

of the pulse is 18TW. The radiation transport code was run with these parameters to a convergence level of 0.1% - the results of the radiation distribution around the interior of the hohlraum can be seen in fig. 3.

Because the albedo is the only remaining degree of freedom in the problem, comparison to experimental data allows the albedo to be calibrated to an effective value. In this case, a simulation albedo of 0.8 yielded a calculated fuel capsule surface temperature of $230.1 \pm 2.7 \, eV$. The measured peak temperature from the Nova experiment was determined to be $227 \pm 3 \, eV$ from fig. 4 - this suggests that 0.8 appears to be an appropriate value for the effective albedo.
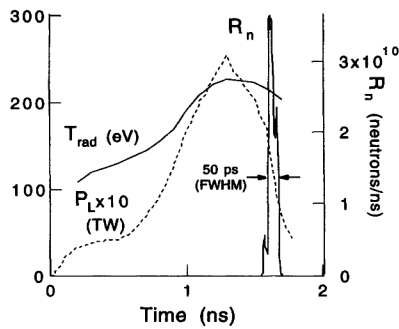
Figure 4 – Experimentally measured hohlraum temperatures in the HEP-1 experiments, reproduced from ref. 8. Also shown is the experimentally measured drive laser ps22 pulse shape.

Modelling the Temporal Evolution of Hohlraum Temperature

After it was known the code could produce realistic results for a given steady power input, it was altered in order to calculate time-dependent radiosity distributions. This is a reasonably straightforward extension of the previous methods. Time-dependence becomes important when the effects of laser pulse shaping are studied. As such, a method of specifying arbitrary pulse shapes and powers was needed. In this implementation, one or more pulse shapes can be specified independently in a transport configuration file. Each beam can then refer to a named profile as it is created.
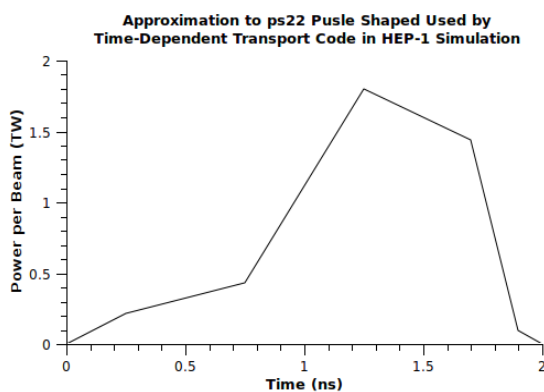

Figure 5 – The approximation to the ps22 pulse shape used in the time-dependent simulation. The shape is defined by a set of points; linear interpolation between the points is used to determine the appropriate beam power at a given time step.

The user defines the pulse shape by supplying a list of points. Each point defines the power of the beam at a given time. By building a list of points in this way, increasingly better approximations to the desired power profile can be created. The time-dependent program then linearly interpolates between the points to determine the applied beam power for each time step. The radiosity balance at each point in time is then solved in the

same manner as before, and the distribution of radiosities is saved for each time step.

As a comparison, the same Nova HEP-1 model was extended by defining a time dependent pulse shape. In the Nova shots, the named ps22 pulse shape was used[9]. The approximation to this pulse shape used is shown in fig. 5, and the resulting simulated capsule surface temperatures are shown in fig. 6.
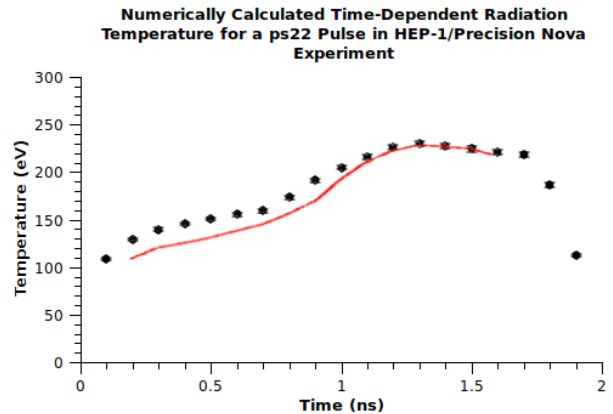

Figure 6 – Time dependent radiation temperature calculation compared with experiment. Points are numerically calculated temperatures over the fuel capsule, with error bars representing non-uniformities. The continuous line is the experimentally measured temperature rescaled from fig. 4.

It can be seen that this is quite a reasonable representation of the experimental results. The form is closer to experimental values around the peak temperatures as this is the region that the albedo was calibrated for; although even for lower temperatures (around 100eV) the divergence from experimental values is quite minimal. This might suggest that the albedo does not vary a great deal over this range of temperature, and that a single value albedo is a quite reasonable approximation. An improved approximation to the ps22 pulse shape might also yield improved results.

Conclusions

This project has developed a basic but capable and user-friendly 3D view-factor code for use in designing high-power laser experiments. It has the ability to model a wide range of user-defined geometries, calculate the appropriate view-factors, and then solve the radiation transport equation in a time-dependent or time-independent manner. It also provides 3D visualisation utilities that can be used to view the results of these operations.

The view factor calculation algorithm has been well tested. Analytically known view-factors can be solved with errors of only a few parts per million using manageably low resolutions. Occlusion is successfully handled, but comes at the price of increased algorithmic complexity. One way to speed up calculation of the view-factor matrix is to implement this as a parallel computation; and this should be relatively straightforward given the nature of the algorithm.

The radiation transport section of the code performed well, despite much of the complexity associated with the underlying physical processes being parameterised in the radiosity equation. It has been shown to reproduce experimental results quite well; as such, it should be able to provide significant insight into the design and performance of new hohlraums for high power laser experiments

References

1. A. Caruso and C. Strangio, J. Appl. Phys. **30**, 1095 (1991)

2. M. Murakami and J. Meyer-ter-Vehn, J. Nucl. Fusion **31**, 1333 (1991)

3. J. MacFarlane, *"Development of a Time-Dependent View Factor Code for Studying Radiation Symmetry in ICF Hohlraums"*. Published by Fusion Technology Institute, University of Wisconsin, call UWFDM-1061 (1998)

4. H. Schenck, *"Heat Transfer Engineering"*, Prentice-Hall Publishing, New Jersey (1959)

5. R. Siegel and J. R. Howell, *"Thermal Radiation Heat Transfer"*, Brooks/Cole Publishing, Belmont CA, 1966

6. R. L. Kauffman. *"X-ray conversion efficiency,"* Laser Program Annual Report, Lawrence Livermore National Laboratory (1986)

7. W. M. Rohsenow, J. P. Hartnett, *"Handbook of Heat Transfer"*, McGraw-Hill (1973)

8. M. D. Cable, S. P. Hatchett, J. A. Caird, Phys. Rev. Letters, **73**(17) 2316 (1994)

9. A. Hammel, C. J. Keane, M. D. Cable, D. R. Kania, J. D. Kilkenny, R. W. Lee, and R. Pasha, Phys. Rev. Lett. **70**, 1263 (1993)

Siegert states in an electric field:
From atoms to molecules

contact : linda@power1.pc.uec.ac.jp, lhamonou01@qub.ac.uk

Linda Hamonou

University of Electro-communications,
1-5-1, Chofu-ga-oka, Chofu-shi, Tokyo, Japan

Shinichi Watanabe

University of Electro-communications,
1-5-1, Chofu-ga-oka, Chofu-shi, Tokyo, Japan

Toru Morishita

University of Electro-communications,
1-5-1, Chofu-ga-oka, Chofu-shi, Tokyo, Japan

Oleg I. Tolstikhin

Russian Research Center "Kurchatov Institute", Kurchatov Square 1, Moscow 123182, Russia

1. Introduction

In a previous work [1], within the single active electron approximation, the Siegert states of atoms in a static uniform electric field, defined as the solutions to the stationary Schrödinger equation satisfying the regularity and outgoing-wave boundary conditions [2], are discussed. In [1], an efficient method to calculate not only the complex energy eigenvalue, but also the eigenfunction for a general class of one-electron atomic potentials is introduced. An exact expression for the transverse momentum distribution of the ionized electrons in terms of the Siegert eigenfunction in the asymptotic region is derived.

In this report, we present an extension of the Siegert states to molecules. The formulation of the computational method in this case requires some modifications.

2. Basic equations

The Schrödinger equation reads
$$H\psi = E\psi. \quad (1)$$

The Hamiltonian for an electron interacting with a model molecular potential $V(\mathbf{r})$ and a static uniform electric field $\mathbf{F}$ directed along the z axis has the form (atomic units are used throughout)

$$H = -\frac{1}{2}\Delta + V(\mathbf{r}) + Fz. \quad (2)$$

We use the parabolic coordinates ξ, η, and φ defined as follows:

$$\xi = r + z, \quad 0 \le \xi \le \infty, \quad (3)$$
$$\eta = r - z, \quad 0 \le \eta \le \infty, \quad (4)$$
$$\varphi = \arctan \frac{y}{x}, \quad 0 \le \varphi \le 2\pi \quad (5)$$

In [1] we have considered the case when the potential has axial symmetry, $V(\mathbf{r}) = V(\xi, \eta)$. Then the solution of Eq. (1) can be sought in the form

$$\psi(\mathbf{r}) = \frac{e^{im\varphi}}{\sqrt{2\pi}}\psi(\xi, \eta), \quad (6)$$

where m is the magnetic quantum number. The function $\psi(\xi, \eta)$ satisfies

$$\left[\frac{\partial}{\partial\eta}\eta\frac{\partial}{\partial\eta} - \frac{m^2}{4\eta} + \mathcal{B}(\eta) + \frac{E\eta}{2} + \frac{F\eta^2}{4}\right]\psi(\xi, \eta) = 0, \quad (7)$$

where the adiabatic Hamiltonian $\mathcal{B}(\eta)$ is given by

$$\mathcal{B}(\eta) = \frac{\partial}{\partial\xi}\xi\frac{\partial}{\partial\xi} - \frac{m^2}{4\xi} - \frac{\xi+\eta}{2}V(\xi, \eta) + \frac{E\xi}{2} - \frac{F\xi^2}{4}. \quad (8)$$

These equations must be supplemented by the regularity and outgoing-wave boundary conditions [1]. For non-zero electric fields, all the eigenstates are unbound, so the eigenvalue E is a complex number,

$$E = \mathcal{E} - \frac{i}{2}\Gamma. \qquad (9)$$

Its real part $\mathcal{E}$ gives the energy of the state, while its imaginary part defines the ionization rate Γ. Equations (7) and (8) are solved using the slow-variable discretization (SVD) method [3] in combination with the R-matrix propagation technique [4]. The numerical procedure is

based on discrete variable representations (DVR) [5] constructed from appropriate classical orthogonal polynomials compatible with the boundary conditions [6]. We refer the reader to [1] for more mathematical and numerical details.

In the general cases, for an arbitrary molecular potential $V(\mathbf{r})$, the variables (ξ, η) and φ cannot be separated. In order to solve the molecular problem we have to take into account a coupling between the different m-components. To this end, we rewrite Eq. (1) in the form

$$\left[\frac{\partial}{\partial\eta}\eta\frac{\partial}{\partial\eta} - \frac{1}{4\eta}\frac{\partial^2}{\partial\varphi^2} + \mathcal{B}(\eta) + \frac{E\eta}{2} + \frac{F\eta^2}{4}\right]\psi(\xi,\eta,\varphi) = 0, \qquad (10)$$

where

$$\mathcal{B}(\eta) = \frac{\partial}{\partial\xi}\xi\frac{\partial}{\partial\xi} - \frac{1}{4\xi}\frac{\partial^2}{\partial\varphi^2} - \frac{\xi+\eta}{2}V(\xi,\eta,\varphi) + \frac{E\xi}{2} - \frac{F\xi^2}{4}. \qquad (11)$$

3. Numerical procedure

In the atomic case [1], the eigenfunctions of the adiabatic Hamiltonian (8) are obtained using the DVR basis constructed from the generalized Laguerre polynomials $L_n^{(|m|)}(s\xi)$ [6], where the scaling factor s defines the extent of the basis functions in ξ. This approach enables one to exactly incorporate the regularity boundary con-

dition $\psi(\xi,\eta)|_{\xi\to 0} \propto \xi^{|m|/2}$ into the formulation. In the molecular case, however, the solution $\psi(\xi,\eta,\varphi)$ contains integer as well as half-integer powers of ξ for $\xi \to 0$, which cannot be represented by a single Laguerre-DVR basis with a fixed m. To resolve this difficulty, we introduce a new variable,

$$\xi = \zeta^2. \qquad (12)$$

Then

$$\mathcal{B}(\eta) = \frac{1}{4\zeta}\left[\frac{\partial}{\partial\zeta}\zeta\frac{\partial}{\partial\zeta} + \left(\frac{1}{\zeta} + \frac{\zeta}{\eta}\right)\frac{\partial^2}{\partial\varphi^2} - 2\zeta(\zeta^2+\eta)V(\xi,\eta,\varphi) + 2E\zeta^3 - F\zeta^5\right]. (13)$$

This transformation allows us to use a single Laguerre-DVR basis with $m = 0$ for the expansion in ζ. The eigenfunctions of $\mathcal{B}(\eta)$ are constructed by using the direct product of the Laguerre-DVR basis in ζ and a sinusoidal basis with periodic boundary conditions in φ.

In the R-matrix theory [7], the space is divided into inner and outer regions. The inner region $0 \leq \eta \leq \eta_c$ is divided into N_{sec} sectors, $0 = \eta_0 < \eta_1 < \cdots < \eta_{N_{\text{sec}}} = \eta_c$. In each sector, we construct the R-matrix basis $\bar{\psi}_n(\xi,\eta,\varphi)$ defined by

$$\left[\frac{\partial}{\partial\eta}\eta\frac{\partial}{\partial\eta} - \mathcal{L} - \frac{1}{4\eta}\frac{\partial^2}{\partial\varphi^2} + \mathcal{B}(\eta) + \frac{\bar{E}_n\eta}{2} + \frac{F\eta^2}{4}\right]\bar{\psi}_n(\xi,\eta,\varphi) = 0, \quad (14)$$

where $\mathcal{L}$ is the Bloch operator,

$$\mathcal{L} = \eta[\delta(\eta - \eta_+) - \delta(\eta - \eta_-)]\frac{\partial}{\partial\eta}. (15)$$

In the atomic problem [1], in order to incorporate the regularity boundary condition $\psi(\xi,\eta)|_{\eta\to 0} \propto \eta^{|m|/2}$, in the first sector Eq. (14) was solved using the DVR basis constructed from the Jacobi polynomials $P_n^{(0,|m|)}(x)$ [6]; in further sectors Legendre polynomials were used. However, in the molecular case the solution contains integer as well as half-integer powers of η for $\eta \to 0$, similarly to the ξ variable. To allow the representation of the solution by

a single Legendre-DVR basis, we need to implement another change of variables in the first sector,

$$\eta = \chi^2. \tag{16}$$

In the outer region, $\eta > \eta_c$, the molecular potential is substituted by a purely Coulomb tail $-Z_{as}/r$. Then the problem becomes exactly separable in parabolic coordinates and reduces to solving uncoupled equations in η [1]. Here the outgoing-wave boundary condition is applied. The R-matrix is propagated from $\eta = 0$ outward, and from $\eta = \eta_c$ inward. By matching the solutions at the right boundary of the first sector, we obtain the Siegert eigenvalue E and eigenfunctions.

Some preliminary results for an H_2^+ molecule aligned along the electric field are presented in the figures. The energy $\mathcal{E}$ and ionization width Γ of the lowest sigma state as function of the field F are shown in Fig. 1. The transverse momentum distribution of the ionized electrons for $F = 0.5$ a.u. is shown in Fig. 2.
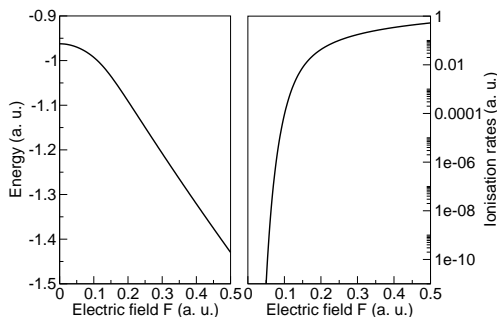
and eigenfunction for a particular Siegert state as a functions of the electric field F for molecules modeled by one-electron potentials.
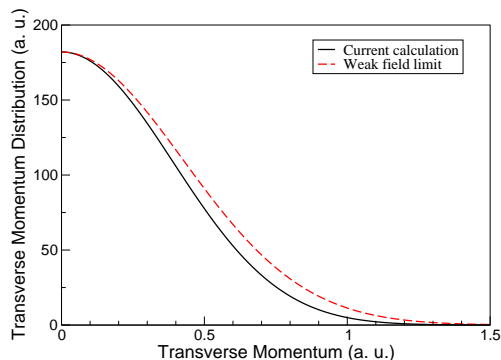

Fig. 2. Transverse momentum distribution as a function of transverse momentum. The current calculation is compared to the weak field limit Gausian defined by $exp(-\frac{K_\perp \sqrt{2|E_0|}}{F})$ with $F = 0.5$ a.u., the electric field, $|E_0|$ the ionisation potential without laser field and $K_\perp$ the transverse momentum.

Fig. 1. Energy and Ionisation rates as a function of electric field F.

4. Conclusion

In this report, we have briefly presented the development necessary to calculate the molecular Siegert states in a static electric field. Starting from an atomic problem enabling the calculation of Siegert states in the single active electron approximation, we have extended the program by reducing the use of the symmetries and including m-coupling to solve the molecular problem. This new method enables one to obtain the eigenvalue

Reference

1. P. A. Batishchev, O. I. Tolstikhin and T. Morishita, sumitted to Phys. Rev. A (2010).
2. A. J. F. Siegert, Phys. Rev. **56**, 750 (1939).
3. O. I. Tolstikhin, S. Watanabe and M. Matsuzawa, J. Phys. B **29**, L389 (1996).
4. K. L. Baluja, P. G. Burke and L. A. Morgan, Comput. Phys. Commun. **27**, 299 (1982).
5. D. O. Harris, G. G. Engerholm and W. D. Gwinn, J. Chem. Phys. **43**, 1515 (1965); A. S. Dickinson and P. R. Certain, J. Chem. Phys. **49**, 4209 (1968); J. C. Light, I. P. Hamilton and J. V. Lill, J. Chem. Phys. **82**, 1400 (1985).
6. O. I. Tolstikhin and C. Namba, *CTBC - A Program to Solve the Collinear three-Body Problem: Bound States and Scattering Below the Three-body Disintegration Threshold*, Research Report NIFS-779 (National Institute for Fusion Science, Toki, Japan, 2003). Available at http://www.nifs.ac.jp/report/nifs779.html.
7. P. G. Burke and K. A. Berrington, *Atomic and Molecular Processes: An R-matrix Approach* (IOP, Bristol, 1993).

Finite Size Effects in High-Intensity QED

Contact *theinzl@plymouth.ac.uk*

T. Heinzl

School of Computing and Mathematics, University of Plymouth
Drake Circus, PL4 8AA, Plymouth, UK

A. Ilderton and M. Marklund

Department of Physics, Umeå University
SE-901 87 Umeå, Sweden

Introduction

Within the next few years lasers are expected to reach unprecedented extremes in power (>10 PW), intensity (>10^{23} W/cm^2) and, accordingly, field strength (>10^{15} V/m). In these regimes, equivalent to concentrating the total solar radiation on a pinhead, both relativistic and quantum effects need to be taken into account. The appropriate theoretical tool is a relativistic quantum field theory, namely strong-field, or high-intensity, quantum electrodynamics (QED). This may also be understood from the fact that one is approaching the QED critical electric field strength[1,2],

$$E_S = \frac{m^2 c^3}{e\hbar} = 1.3 \times 10^{18}\,\text{W/m}\,, \qquad (1)$$

which depends on the fundamental constants of both relativity, c, and quantum mechanics, $\hbar$. Beyond this Sauter-Schwinger limit any laser turns into a pair creation machine[3], as the energy gain of an electron over a Compton wavelength equals its rest mass.

Like any quantum field theory, high-intensity QED is characterised by its particle content. Ordinary photons (Fig. 1, wavy line) serve as the usual virtual exchange bosons or as real particles probing the external field given by the laser.

Figure 1: Wavy line: Probe photon; dashed line: laser photon.

The associated laser photons (Fig.1, dashed line), on the other hand, need in general not be explicitly shown. They rather play an 'auxiliary' role by 'dressing' the electrons whereupon these become effective particles, represented by the double line in Fig. 2. Formally, they are given by the Volkov solution[4] of the Dirac equation in a plane wave field, $F^{\mu\nu} = F^{\mu\nu}(k.x)$, where k is the wave four-vector and $k.x = \omega t - kz$ the invariant phase (assuming propagation along the z-axis).
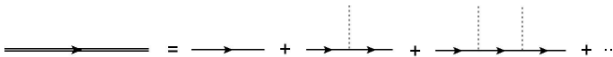

Figure 2: 'Dressed' Volkov electron.

The strength of the laser field is measured by the dimensionless laser amplitude,

$$a_0 \equiv \frac{eE\lambda_L}{mc^2}\,, \qquad (2)$$

the energy gain of a probe electron in the ambient electric field E across a laser wavelength $\lambda_L = 2\pi c/\omega$, divided by the electron rest energy[1]. Defining a dimensionless electric field and frequency via

$$\epsilon \equiv E/E_S\,, \quad \nu \equiv \hbar\omega/mc^2\,, \qquad (3)$$

one may alternatively write $a_0 = \epsilon/\nu$. For a laser one has $\epsilon < 1$, an upper bound imposed by the Sauter-Schwinger limit, which implies that $a_0 < 1/\nu < 10^6$ for an optical laser. For the Vulcan-10PW and Extreme Light Infrastructure (ELI) facilities one expects $a_0 \approx 10^2$ and $a_0 \approx 10^3$, respectively. The parameter a_0 also serves as a characteristic of the Volkov electrons of Fig. 2. They acquire a quasi-momentum given by[2]

$$q_\mu = p_\mu + \frac{a_0^2 m^2}{2k \cdot p}\,k_\mu\,, \qquad (4)$$

with a longitudinal addition, proportional to a_0^2, to the asymptotic particle momentum p[6,7]. Upon squaring one recovers

$$q^2 = m^2(1 + a_0^2) \equiv m_*^2\,, \qquad (5)$$

the celebrated intensity dependent mass shift of an electron in a laser background first discovered by Sengupta[6] and thoroughly discussed by Kibble[8]. The mass shift (5) may be understood in purely classical terms. Solving the Lorentz equation for an electron in an infinite plane wave (IPW) one finds the momentum as a function of proper time, $p = p(\tau)$. The quasi-momentum (4) is then the proper time average of $p(\tau)$, taken over a laser period, the asymptotic momentum p serving as an initial condition.

With the basic intensity, or a_0, dependence of the Volkov electrons identified we may use their graphic representation (Fig. 2) together with a probe photon line from Fig. 1 to build the 'fundamental' vertex of laser-induced strong-field QED. Its Feynman graph is depicted in two different ways in Fig. 3.
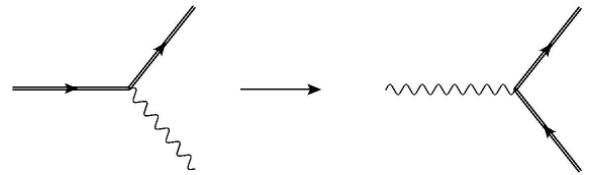

Figure 3: Two versions of the basic strong-field QED interaction, viewed as transition amplitudes, represent nonlinear Compton scattering (left) and stimulated pair production (right). They are related by crossing symmetry.

Several comments are in order. The vertex is fundamental in terms of Volkov electrons but, once expanded via Fig. 2 it becomes an infinite series in terms of diagrams with more and more laser photons. The Volkov representation thus is a rather economic resummation of many-particle tree diagrams and as such is *nonperturbative* in the coupling e. Viewing the graphs of Fig. 3 as S-matrix elements (transition amplitudes) rather than vertices the two diagrams acquire different meanings. The left-hand graph describes nonlinear Compton scattering (NLC) or, equivalently, the emission of a photon by an electron in an intense wave[9,10]. (See [11] for a recent reanalysis and update.). Expanding the Volkov lines according to Fig. 2 yields a sum over all processes of the form

---

[1] This can be written in a manifestly Lorentz and gauge invariant way[5].

[2] We adopt natural units, $\hbar=c=1$, in what follows.

$$e + n_1\gamma_L \rightarrow e' + \gamma' , \qquad \text{(NLC)} \qquad (6)$$

labelled by n_1, the number of laser photons involved. The right-hand graph of Fig.3 represents stimulated pair production (sPP) with the 'stimulating' photon, γ', apparently decaying into a Volkov electron-positron pair. Again, this may be viewed as summing all processes,

$$\gamma' + n_2\gamma_L \rightarrow e^+ + e^- , \qquad \text{(sPP)} \qquad (7)$$

over n_2. Whenever the laser photon numbers n_1, $n_2 > 1$, the process in question is called nonlinear. The linear processes ($n_1 = n_2 = 1$) are standard Compton scattering[12] and Breit-Wheeler pair production[13]. In the limit of vanishing external field (formally obtained by setting $n_1 = n_2 = 0$), i.e. for bare rather than dressed electrons, both scattering processes are forbidden by energy-momentum conservation.

The two strong-field processes (6) and (7) were simultaneously observed in the famous experiment SLAC E-144[14,15,16] with values of n_1 and n_2 up to five. In particular, about 10^2 positron events were recorded, realising the 'creation of matter from light' for the first time. The experimental results have been claimed to be consistent with the theory as developed in [9,10]. It should, however, be emphasised that this theory was explicitly worked out only for plane waves of infinite temporal and spatial extent. In general, however, such an IPW does not represent a realistic laser beam which typically is pulsed (hence of finite time duration) and also localised in space, both longitudinally and transversally, as measured by Rayleigh length, z_R and waist, w_0. It thus seems appropriate to address possible modifications of the theory and its predictions caused by finite spatio-temporal size effects.

Finite Size Effects in Nonlinear Compton Scattering

As already noted, strong-field QED in laser backgrounds relies heavily on the existence of the Volkov solution in a plane wave field, $F^{\mu\nu} = F^{\mu\nu}(\varphi)$, $\varphi = k.x$. The wave in question, however, may be an *arbitrary* function of φ. Hence it need not be of infinite extent in φ as for an IPW, but may be a finite wave train[17] or pulsed with a smooth envelope. We will generically refer to such configurations as pulsed plane waves (PPWs). A nice example of the latter has recently been discussed by Mackenroth et al.[18] with a pulse profile which we slightly generalise to

$$f(\phi) = \begin{cases} \sin^K(\phi/2N)\sin(\phi + \phi_0) , & 0 \le \phi \le 2\pi N \\ 0 , & \text{otherwise} \end{cases} \qquad (8)$$

allowing for an additional 'carrier phase' φ_0 between the oscillatory sine part and the $\sin^K$ envelope[3]. The integer N counts the number of cycles within the pulse, see Fig. 4.
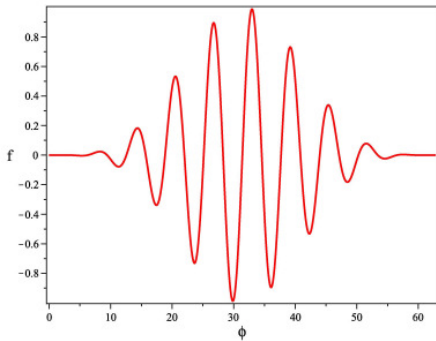

Figure 4: Pulse profile (8) for K=4, N=10 and φ_0= 0.

---

[3] Mackenroth et al.[18] used $K = 4$ and were particularly interested in the carrier phase and its consequences. For our purposes, though, it is sufficient to set φ_0= 0.

Soon after the mass shift had been (re)discovered in the sixties there was a discussion on whether it is really observable in view of the somewhat unphysical nature of an IPW. Kibble[8] has convincingly argued (using an exponentially damped wave) that all that is required are pulses that are 'sufficiently' long. Quantitatively, this translates into having a small width $\Delta\omega$ in laser frequency, $\Delta\omega \ll \omega$, which just corresponded to the state of the art for lasers in the sixties[4]. In terms of the invariant phase this may be reformulated as

$$\Delta\phi/2\pi \sim N \gg 1 , \qquad (9)$$

where $\Delta\varphi$ is the width in φ, taken to be $2\pi N$ for the pulse (8). So we expect an IPW to be a reasonable model in the large-N limit, i.e. when the laser pulse contains many cycles. The SLAC E-144 100 TW laser pulse had a duration of 2 ps corresponding to $N \approx 10^3$ which should be close to the IPW regime. For current ultra-short pulses of, say, 10 fs, however, one clearly enters the few-cycle regime, $1 < N < 10$, where Kibble's criterion (9) ceases to be valid. This suggests that the idea of an effective mass arising as an averaging effect due to the electron quiver motion may become questionable. As the Volkov solution remains valid also for pulses it is possible to test the significance of mass shift effects quantitatively. While the IPW S-matrix elements[9,10] can be extended to the PPW case, there is an alternative route available for NLC in the classical (Thomson) limit ($v \ll 1$). This is to calculate the classical Larmor radiation (or bremsstrahlung) of an electron accelerated by the wave. This has been done in [19] where the validity of the classical limit was also checked explicitly. The complete IPW spectrum of the scattered photons is shown in Fig. 5.
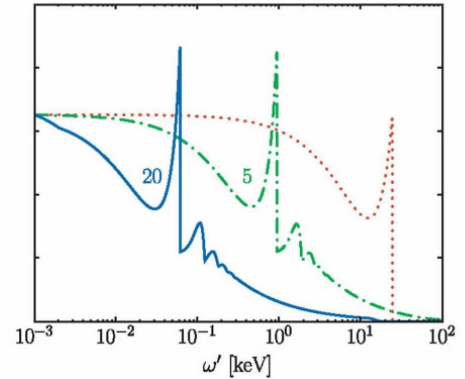

Figure 5: Total photon emission spectrum (in arbitrary units) for NLC, summed over all harmonics, as a function of scattered frequency, $\omega' = m v'$. Parameter values: $a_0 = 5$ and $a_0 = 20$ as indicated, $\gamma = 80$. The dotted curve corresponds to $a_0 \rightarrow 0$, i.e. standard ('linear') Compton scattering. (From [19].)

The following generic intensity effects may be noted: (i) the kinematic $n_1 = 1$ Compton edge (represented by the principal peak in each of the spectra) is red-shifted, when a_0 is nonzero, to the value

$$\nu'_1(a_0) = \frac{\nu e^{2\zeta}}{1 + a_0^2 + 2\nu e^\zeta} \simeq \frac{4\gamma^2\nu}{1 + a_0^2} . \qquad (10)$$

Here, ζ denotes rapidity i.e. $e^\zeta = \gamma\,(1+\beta)$, with γ and β the standard Lorentz factors for the incoming electron. The last identity in (10) is valid when $1 \ll \gamma \ll 1/4\nu$.

(ii) There are smaller peaks beyond the $n_1 = 1$ edge ($v' > v'_1$) corresponding to higher harmonics, $n_1 > 1$. The associated spectral ranges are given by $n_1 v < v' < v'_{n1}$, where v'_{n1} is given by (10) with v replaced by $n_1 v$.

[4] Recall that an IPW corresponds to a delta function, $\delta(\omega)$, hence zero width.

Higher harmonics, i.e. scattered photons with frequencies $\nu' > \nu'_1$, have been observed in the SLAC E-144 experiment together with a 'shoulder' corresponding to the $n_1 = 2$ peak (see Fig. 39 in [16]). This was a high energy experiment with 46.6 GeV electrons ($\gamma\nu \approx 0.4$), the Compton edges accordingly of similar magnitudes, $m\nu'_1 = 29$ GeV, $m\nu'_2 = 36$ GeV.

To analyse the effects of finite pulse duration let us concentrate on the first harmonic, $n_1 = 1$. For an IPW this is plotted in Fig. 6 as a function of scattered frequency. The latter has been rescaled by $\nu'_0 = \nu \, e^{2\zeta}$ such that the linear and nonlinear edges are located at 1 and $1/(1+ a_0^2)$, respectively.
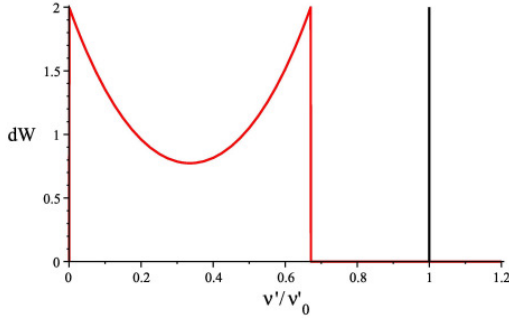
Figure 6: IPW photon emission spectrum (in arbitrary units) corresponding to the first harmonic ($n_1 = 1$), for $a_0 = 0.7$, as a function of rescaled frequency. Note the spectral gap between nonlinear and linear Compton edges (red and black vertical lines, respectively).

The first harmonic signal for an IPW has a sharp edge and there is no signal beyond. Thus, there is a characteristic spectral gap between the nonlinear and linear kinematic edges. This, however, changes significantly for PPWs.
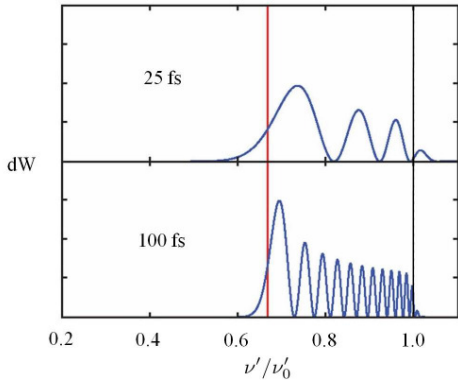

Figure 7: PPW photon emission spectra (in arbitrary units) corresponding to the first harmonic ($n_1 = 1$), for $a_0 = 0.7$, as a function of rescaled frequency. Upper panel: Pulse duration 25 fs. Lower panel: Pulse duration 100 fs. (From [19].)

Fig. 7 shows the first harmonic signal in the same rescaled frequency range for pulse durations of 25 fs and 100 fs. One clearly observes a strong 'leakage' of the signal into what was previously the spectral gap. The number of oscillations seems to be linearly increasing with pulse duration, from $N = 3$ to $N = 12$. This suggests that the IPW limit is obtained by having destructive interference of rapid oscillations, an issue which clearly deserves further study. In the very same frequency domain, the signal will be further distorted by the presence of higher harmonics, $n_1 > 1$, recall the discussion of Fig. 5. Thus, for short pulses, it should be rather difficult to observe the red-shift of the Compton edge.

Let us conclude this section with a few words on the effect of the transverse beam profile. There are two complementary cases corresponding to a strong and weak laser focus, respectively (see Fig. 8). The spatial scale to be compared to in both cases is

the electron beam radius, r_b, which, typically, will be of the order of 10 microns.
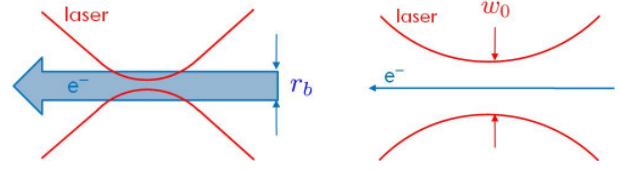
Figure 8: Schematic sketch of laser beams strongly and weakly focused in comparison to the electron beam. Left panel: strong focus, $w_0 < r_b$. Right panel: weak focus, $w_0 \gg r_b$.

For a tight focus, (waist size $w_0 < r_b$, usually required for large $a_0 \gg 1$) the electrons are rather sensitive to the finite transverse extension of the laser beam, and finite size effects will be important. On the other hand, a weakly focussed laser ($w_0 \gg r_b$) will appear approximately as a plane wave (of finite longitudinal extent) to the electrons. In this case, finite size effects should be minor, and strong-field QED based on the Volkov solution should be a reasonable approximation. Indeed, one finds that the strongly focussed case generically leads to finite size dominated, broad and unstructured spectra, while for a sufficiently weak focus spectral substructure remains identifiable [19].

The SLAC experiment had a laser waist $w_0 \approx 5$ microns and an electron beam radius $r_b \approx 60$ microns $> w_0$, corresponding to the scenario of Fig. 8, left panel. This suggests that effects due to the finite transverse extension of the laser beam should have been significant. In the analysis of the experiment this was dealt with by the 'adiabatic approximation' that the IPW theory is valid within small space-time cells covering the laser focus. In each such cell the instantaneous and local value of a_0 (i.e. photon density) as well as the electron density were assumed to be constant (cf. App. A.5 of [16]). It seems difficult to assess the validity of this assumption.

Finite Size Effects in Stimulated Pair Production

As stated in the introduction, the sPP process (7) has also been observed at SLAC by (i) detecting about 10^2 positron signals and (ii) finding a nonlinear dependence on the number of laser photons[15,16]. Note that, unlike NLC (6) sPP is a threshold process. For an IPW, energy-momentum conservation involves the electron and positron quasi-momenta, $k' + n_2 k = q + q'$, which makes the threshold dependent on the *effective* mass (5), requiring that the usual Mandelstam variable $s > 4m_*^2$ or, in terms of dimensionless parameters and assuming a head on collision,

$$n_2 \geq \frac{1 + a_0^2}{\nu\nu'} \ . \tag{11}$$

Clearly, the minimum n_2 increases with a_0 and decreases with the energy, ν', of the 'stimulating' photon which, in the SLAC experiment, was obtained by NLC back-scattering resulting in $m\nu' \approx 29$ GeV for $n_1 = 1$ or $m\nu' \approx 36$ GeV for $n_1 = 2$. In the parameter range $0.2 < a_0 < 0.4$ SLAC E-144 determined a positron production rate R which was well fitted by an intensity dependence according to the power law

$$R \sim a_0^{2n} \ , \quad n = 5.1 \pm 0.2\,(\text{stat})^{+0.5}_{-0.8}\,(\text{syst}) \ , \tag{12}$$

clearly indicating an exponent $n = 5$ (cf. Fig. 44 of [16]). This has been interpreted as the requirement of having 5 laser photons participating for the SLAC a_0 range just given. Note, however, that the processes (6) and (7) were both happening repeatedly and simultaneously in the space-time volume (given by the overlap of laser and electron beams) and thus were impossible to disentangle experimentally, and so the n from

(12) should be a linear combination, $n = n_1 + n_2$, stemming from *both* processes. With $n_1 = 1$ producing a 29.1 GeV photon, the situation here is a little subtle: according to (11), the required number of *additional* photons required to produce a pair changes from $n_2 = 4$ to $n_2 = 5$ at $a_0 \approx 0.22$. Hence, the SLAC results seem to exhibit some 'sub-threshold' production of pairs. Note also that for pairs produced when $a_0 < 0.22$, both (11) and the 'linear' ($a_0 = 0$) threshold predict $n_2 = 4$ for the photon number. Thus it seems that $n_1 = 1$ and $n_2 = 4$ cannot give an unambiguous identification of effects caused by the mass shift. The upshot then is the following. While SLAC E-144 has clearly identified *nonlinear* behaviour (n_1, $n_2 > 1$) the a_0 values may have been too small for a definite identification of intensity effects in sPP such as the shifted threshold. Hence, Sengupta's mass shift[6,8] remains unobserved.

In light of the above, we now turn to consider the effects of finite pulse duration[20]. Again, also for sPP, strong-field QED based on Volkov solutions remains valid for pulses in $\varphi = k.x$. The main consequences are summarised in Fig. 9 showing a triple differential sPP rate, d^3W, assuming the pulse (8) with $K = 0$, i.e. a finite wave train with no envelope.
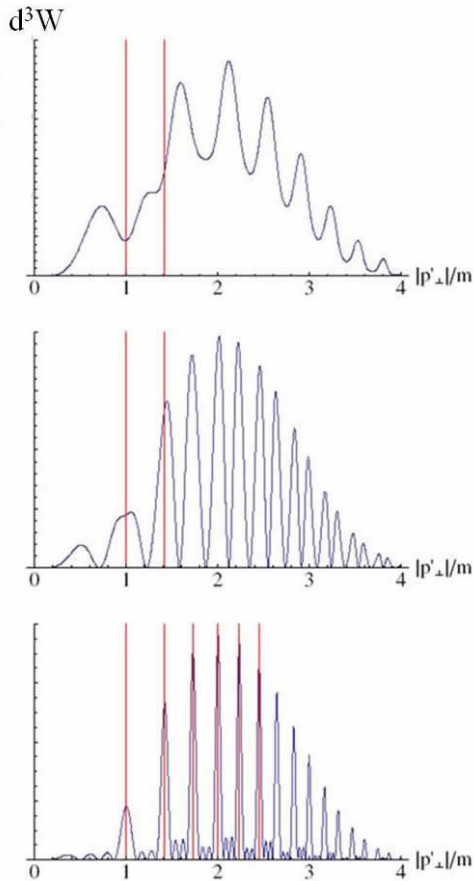
Figure 9: Triple differential sPP rate (arbitrary units) as a function of transverse positron momentum. Circular polarisation, $a_0 = 2$, mv' = 250 GeV, N = 1, 2 and 4 cycles per pulse (descending), i.e. pulse durations of 4 fs, 8 fs and 16 fs, respectively. Vertical lines show the IPW limit (a delta comb).

Most interestingly, one observes another 'leakage' phenomenon very much analogous to NLC (cf. Figs. 6 and 7). For an IPW the rate is given by delta comb resonances. These are shown in Fig. 9 as vertical red lines which begin, for our parameters, at a threshold value of $|p'_\perp|/m = 1$ where $p'_\perp$ denotes the transverse positron momentum. For a PPW, however, the signal 'leaks' into the transverse momentum regime below, in other words, there is *sub-threshold* behaviour, i.e. for centre-of-mass energies below $2m_*$.

This behaviour is most pronounced when the number N of cycles per pulse defined in (9) is small (first panel of Fig. 9). In the large-N limit the IPP features are recovered (last panel of Fig. 9). Thus, an unambiguous observation of the mass shift in sPP (in terms of a blue-shifted sPP threshold) will require $a_0 \gg 1$, hence short pulses, and, accordingly, a significant control of finite pulse duration effects.

We remark that the rapid oscillations appearing in both Fig. 7 and Fig. 9 are a typical signal of finite (temporal) pulse duration: they are also observed in the spectra of pairs produced in the focus of colliding lasers, modelled by oscillating electric fields[21,22].

Conclusions

We have discussed two basic processes of high-intensity QED, nonlinear Compton scattering (NLC) and stimulated pair production (sPP). These processes are related by crossing symmetry and hence show some similar features. If the laser is modelled as an infinite plane wave, intensity effects manifest themselves as clear and unambiguous signals, ultimately caused by the intensity dependent mass shift, $m^2 \to m^2 (1 + a_0^2) = m_*^2$. For both processes, these signals are given by spectral shifts in the allowed kinematic regions compared to the 'linear' ($a_0 = 0$) processes. For NLC one finds a red-shift of the upper Compton edge in the spectrum of emitted photons. For sPP, on the other hand, there is a blue-shift of the sPP threshold directly proportional to m_*. Both effects increase with intensity, hence with laser amplitude, a_0, which seems to favour having large a_0. However, the standard way of boosting a_0 is temporal pulse compression. On the theoretical side this implies trading the infinite plane wave model for a more realistic finite pulse model which is reasonably straightforward. In such models, pulse duration is conveniently measured by the number N of laser cycles per pulse. For small $N = 1...10$, the spectral shifts characterising the infinite plane wave model get washed out, the more so the smaller N. It thus seems that an unambiguous identification of intensity effects on particle spectra will require a delicate balance between having sufficiently large $a_0 \gg 1$ (high compression) and sufficiently long pulses (low compression). As these requirements are somewhat in opposition of each other, a substantial amount of fine-tuning will be necessary. Nevertheless, it is possible to identify parameters which help to expose various intensity effects[19], and we are optimistic that their observation will remain feasible.

References

1. F. Sauter, Z. Phys. **69** (1931) 742

2. J.S. Schwinger, Phys. Rev. **82** (1951) 664

3. A.M. Fedotov, N.B. Narozhny, G. Mourou and G. Korn, arXiv:1004.5398 [hep-ph]

4. D. Volkov, Z. Phys. **94** (1935) 250

5. T. Heinzl and A. Ilderton, Opt. Commun. **282** (2009) 1879

6. N. Sengupta, Bull. Math. Soc. (Calcutta), **44** (1952) 175

7. V.B. Berestetsky, E.M. Lifshitz and L.P. Pitaevsky, *Quantum Electrodynamics* (Course Of Theoretical Physics, Vol. 4), Pergamon, Oxford (1982)

8. T.W.B. Kibble, Phys. Rev. **138** (1965) B740

9. A.I. Nikishov and V.I. Ritus, Zh. Eksp. Teor. Fiz. **46** (1963) 776 [Sov. Phys. JETP **19** (1964) 529]

10. N.B. Narozhnyi, A.I. Nikishov and V.I. Ritus, Zh. Eksp. Teor. Fiz. **47** (1964) 930 [Sov. Phys. JETP **20**, 622 (1965)]

11. C. Harvey, T. Heinzl and A. Ilderton, Phys. Rev. A **79** (2009) 063407

12. A.H. Compton, Phys. Rev. **21** (1923) 483

13. G. Breit and J.A. Wheeler, Phys. Rev. **46** (1934) 1087

14. C. Bula *et al.*, Phys. Rev. Lett. **76** (1996) 3116

15. D.L. Burke *et al.*, Phys. Rev. Lett. **79** (1997) 1626

16. C. Bamber *et al.*, Phys. Rev. D **60** (1999) 092004

17. R.A. Neville and F. Rohrlich, Phys. Rev. D **3** (1971) 1692

18. F. Mackenroth, A. Di Piazza and C.H. Keitel, arXiv:1001.3614 [physics.acc-ph]

19. T. Heinzl, D. Seipt and B. Kämpfer, Phys. Rev. A **81** (2010) 022125

20. T. Heinzl, A. Ilderton and M. Marklund, arXiv:1002.4018

21. F. Hebenstreit, R. Alkofer, G.V. Dunne and H. Gies, Phys. Rev. Lett. **102** (2009) 150404

22. C.K. Dumlu, arXiv:1006.3882 [hep-th]

Multi-electron dynamics on the femtosecond time-scale

Contact *m.lysaght@qub.ac.uk*

**M. A. Lysaght, S. Hutchinson and H. W. van der Hart**

Centre for Theoretical Atomic, Molecular and Optical Physics, Queen's University Belfast, Belfast BT7 1NN, UK

Introduction

The recent emergence of attosecond light sources promises to provide deeper insight into ultrafast *correlated* dynamics *between* electrons in complex matter [1]. In order to accurately describe such dynamics, theoretical methods which go beyond a single-active-electron (SAE) description of the laser-atom interaction are required. One method that offers such a description is the time-dependent *R*-matrix (TDRM) method, recently developed at Queen's University Belfast [2]. In the first part of this report, we use the TDRM method to investigate ultrafast correlated dynamics between two 2p electrons inside C⁺. We show that, by selecting laser pulse parameters carefully it is possible to choose the nature of the correlated dynamics between these two 2p electrons. In the second part of the report we investigate how the choice of dipole gauge can affect the convergence of TDRM calculations. Our findings help to verify that for the interaction of the laser field with a multi-electron atom, the laser field near the nucleus is in practice best described using the length form of the dipole operator.

Time-dependent R-matrix theory

In TDRM theory, the time-dependent Schrödinger equation is solved by dividing the position space of the atomic electrons into an inner and outer region with the boundary of the inner region at radius $r = a_0$ and the boundary of the outer region at radius $r = a_p$ (see figure 1) [3]. In the inner region, electron exchange and correlation effects between the ejected electron and the remaining electrons are important and atom-laser Hamiltonian matrix elements are calculated explicitly. In the outer region only one electron is present, which besides experiencing the laser field directly, is aware of the remainder of the atomic system only via long-range multi-pole interactions.
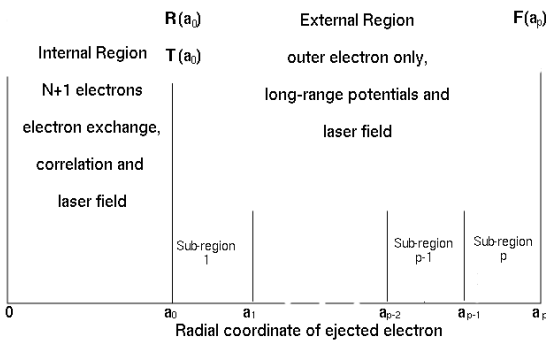
**Figure 1. Division of the position space of the atomic electrons in TDRM theory.**

In the inner region, an *R*-matrix basis expansion of the wave function is adopted. Using a linear solver at each time step, we can calculate the *R*-matrix, **R**, on the boundary, $r = a_0$, of this region and also calculate an inhomogeneous *T*-vector, **T**, both as defined in [2].

In the outer region $a_0 \leq r \leq a_p$, a set of coupled differential equations describing the motion of the ejected electron in the presence of the light field needs to be solved at each time step.

We achieve this by sub-dividing this region into *p* sub-regions and propagating the *R*-matrix and *T*-vector across them from $r = a_0$ to $r = a_p$ as shown in figure 1. The *R*-matrix and *T*-vector at $r = a_p$ can be used to propagate the wave function (**F** in figure 1) backwards across the *p* sub-regions with the assumption $\mathbf{F}(a_p) = 0$. This propagated wave function then provides the starting point for the calculation at the next time step.

Influencing correlated two-electron dynamics inside C⁺

We propose a pump-probe scheme in which we are able to influence the nature of the correlated dynamics occurring between two electrons [4]. Our scheme is similar to a pump-probe scheme used in a previous study of collective electron dynamics [5]. The basic features of the scheme are presented in figure 2.
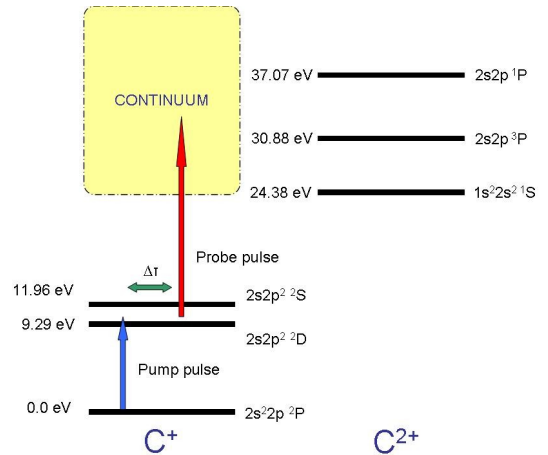

Figure 2. Pump-probe scheme. The pump pulse has a photon energy, ω_1 = 10.0 eV in order to be near resonant with the ²S and ²D states, but with different detunings. The time-delayed probe pulse has a photon energy, ω_2 = 21.8 eV to transfer population above the C²⁺ 2s2p ³P ionization threshold.

We consider C⁺ in its ground state with total magnetic quantum number M=0. The ion is excited by an XUV pulse linearly polarized in the *z* direction into a superposition of the excited 2s2p² ²S and ²D states. The repulsion between the two 2p electrons results in interference between the two excited LS states, which occurs on a time scale of 1-2 femtoseconds. By subsequently ionizing C⁺ with a time delayed ultrashort XUV pulse and analyzing the properties of the ejected electron we are able to probe the interference and investigate the role of electron-electron interactions in the transition from ultrashort-pulse excitation to long-pulse excitation.

Results

To describe the correlated dynamics of the 2p electrons in terms of the dynamics of individual electrons, we transform from the LS-coupled basis to the uncoupled | 2p_{m1} 2p_{m2} > basis, in which the roles of magnetic sub-states becomes more transparent.

Figure 3 shows the 2-dimensional (2D) momentum distributions of the ejected electron obtained for three separate pump pulse durations and for three delays of the probe pulse.
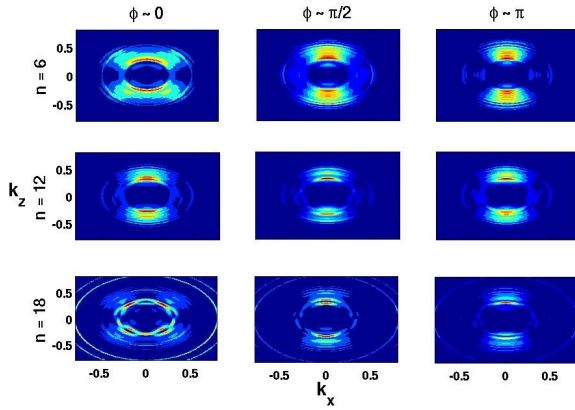
Figure 3. 2D momentum distributions associated with the residual C^{2+} ions left in the 2s2p ^{3}P state in the $k_x k_z$ plane for the ejection of an electron from the pumped C^+ ion for pump pulse durations of n = 6, 12 and 18 cycles. φ corresponds to the phase of the breathing motion.

The first time delay (φ ~ 0) between the pulses corresponds to a minimum of the $| 2p_0\ 2p_0 >$ population. The third delay (φ ~ π) corresponds to a maximum $| 2p_0\ 2p_0 >$ population and the second delay (φ ~ π/2) corresponds to the midpoint between these two delays. Figure 3 clearly shows the dominant emission of |m| = 1 electrons for the n = 6 and n = 18 cycle pump pulses for delays at which the $| 2p_0\ 2p_0 >$ is at a minimum. At the third time delay, the probe pulse interacts with the wave-packet when the $| 2p_0\ 2p_0 >$ is at a maximum. The dominance of the m = 0 electron emission along the laser polarization axis is clearly evident at this delay. This behavior indicates that the wave-packet is undergoing a breathing motion in which it oscillates between two distinct angular distributions. The wave-packet will oscillate between these distributions after the end of the pulse with a period of 1.5 fs, determined by the energy separation between the ^{2}S and ^{2}D states. For a wave-packet prepared by the n = 12 cycle pump pulse, however, it is more difficult to find evidence of correlated electron dynamics. The dominance of population in the ^{2}D state means that the breathing motion between the two angular distributions only forms a small part of the excitation into the 2s2p^2 configuration.

Figure 3 shows that by carefully choosing the duration of the excitation pulse, it is possible to select the nature of the excitation of the 2p^2 configuration. For certain excitation pulse durations, the excitation will be dominated by a single LS coupled state, but for other pulse durations, the excitation will be dominated by a breathing motion between uncoupled states.

Choice of dipole gauge in the TDRM method

One of the main challenges in theoretical atomic physics is the description of multi-electron dynamics in intense laser fields. A full description of multi-electron dynamics is computationally demanding and, consequently, approximations must be made. In the TDRM method we use a restricted basis set to describe the system. As a result of this approximation, the choice of dipole operator gauge used to describe the laser-atom interaction has a significant effect on the outcomes.

We investigate the optimum choice of gauge for use with the TDRM method by considering a test case of multi-photon ionization of He using both the dipole length gauge and the dipole velocity gauge [6]. The basis sets we consider range from using only the 1s orbital to describe He$^+$, to including the 1s, 2s, 2p, 3s, 3p and 3d orbitals (and pseudo-orbitals) in the basis set for He$^+$.

Results

Figure 4 shows the ionization probabilities as a function of time for a laser with a photon energy ω = 6.53 eV for both the length gauge (solid lines) and velocity gauge (dashed lines) when using two different basis sets. The length gauge provides a more consistent result, with the velocity gauge showing a large discrepancy between each basis set. Ultimately both gauges converge to the same result as additional orbitals and pseudo-orbitals are added to the basis set.
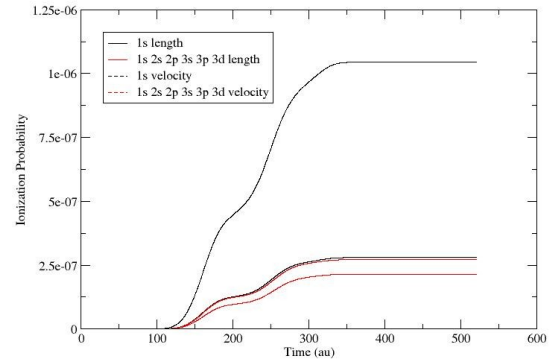
Figure 4. Helium ionization probabilities using the length and velocity gauges for a laser pulse with photon energy 6.53 eV and peak intensity 2 10^{13} W cm^{-2}.

As the length gauge is found to have a higher consistency with respect to the number of orbitals in the basis set, we consider the length gauge to be the preferred choice of gauge. Analysis of multiphoton matrix elements suggests this is a result of a higher sensitivity to high energy processes in the velocity gauge.

Conclusion

In the first part of this report we have used the recently developed TDRM method to propose a technique that may provide the possibility of influencing the field-free evolution of multi-electron wave-packets. In the near future, we intend to investigate more elaborate laser pulse schemes which will allow more control over the population of the excited states during the pumping stage. We also intend to extend this study to more complex configurations. Such studies may lead to further insight into the fundamental connection between atomic structure and correlated multi-electron dynamics.

In the second part of the report we investigated how the choice of dipole gauge can affect TDRM calculations and have shown that for a laser field interacting with a multi-electron atom close to nucleus, the length form of the dipole operator appears to be a better choice of gauge. This is particularly the case for the finite basis set calculations employed in the TDRM inner region.

Acknowledgements

References

1. T. Morishita, S. Watanabe and C. D. Lin, *Phys. Rev. Lett.* **98**, 083003 (2007).

2. M. A. Lysaght, H. W. van der Hart and P. G. Burke, *Phys. Rev. A* **79**, 053411 (2009).

3. P. G. Burke and K. A. Berrington, *Atomic and Molecular Processes: An R-matrix approach* (Bristol: IOP) (1993).

4. M. A. Lysaght and H. W. van der Hart, *J. Phys. B* **43**, 121001 (2010).

5. M. A. Lysaght, P. G. Burke and H. W. van der Hart, *Phys. Rev. Lett.* **102**, 193001 (2009).

6. S. Hutchinson, M. A. Lysaght and H. W. vand der Hart, *J. Phys. B* **43**, 095603 (2010).